

1 **High-Resolution UV Absorption Cross-section Measurements of  $^{32}\text{S}$ ,  $^{33}\text{S}$ ,**  
2  **$^{34}\text{S}$ , and  $^{36}\text{S}$  Sulfur Dioxide for the  $\tilde{B}^1B_1\text{-}\tilde{X}^1A_1$  Absorption Band**

3 **Y. Li<sup>1</sup>, S. O. Danielache<sup>1</sup>, Y. Endo<sup>2</sup>, S. Nanbu<sup>1</sup>, Y. Ueno<sup>2,3,4</sup>**

4 <sup>1</sup>Department of Materials and Life Science, Faculty of Science and Technology, Sophia  
5 University, Japan

6 <sup>2</sup>Department of Earth and Planetary Sciences, Tokyo Institute of Technology, Tokyo, Japan

7 <sup>3</sup>Earth-Life Science Institute, Tokyo Institute of Technology, Tokyo, Japan

8 <sup>4</sup>Institute for Extra-cutting-edge Science and Technology Avant-garde Research (X-star),  
9 Super-cutting-edge Grand and Advanced Research (SUGAR) Program, Japan Agency for  
10 Marine-Earth Science and Technology (JAMSTEC), Yokosuka, Japan

11 Corresponding author: Yuanzhe Li ([liyuanzhe@eagle.sophia.ac.jp](mailto:liyuanzhe@eagle.sophia.ac.jp))

12 **Key Points:**

- 13 • We report measured cross-sections of  $^{32}\text{SO}_2$ ,  $^{33}\text{SO}_2$ ,  $^{34}\text{SO}_2$ ,  $^{36}\text{SO}_2$  for the  $\tilde{B}^1B_1\text{-}\tilde{X}^1A_1$   
14 absorption band over the wavelength range 240 to 320 nm at a resolution of  $0.4\text{ cm}^{-1}$ .  
15 • A least absolute deviation linear regression method was applied to calculate the cross-  
16 sections, and the error bars on the measured cross-sections ranged between 3 and 10%.  
17 • Reported absorption cross-sections predict relatively small mass-independent  
18 fractionation ( $^{33}E = -0.8\pm 0.2\%$  and  $^{36}E = -4.0\pm 0.4\%$ ) during  $\text{SO}_2$  photoexcitation for  
19 top of the atmosphere solar spectra.  
20

## 21 Abstract

22 High-resolution and high-precision spectrum data presents a challenging measurement. We  
23 report newly measured ultraviolet absorption cross-sections of  $^{32}\text{SO}_2$ ,  $^{33}\text{SO}_2$ ,  $^{34}\text{SO}_2$ , and  $^{36}\text{SO}_2$   
24 for the  $\tilde{B}^1B_1-\tilde{X}^1A_1$  band over the wavelength range 240 to 320 nm at a resolution of  $0.4\text{ cm}^{-1}$ .  
25 The resolution is improved by 20 times compared to a previous study (Danielache et al., 2012).  
26 A least absolute deviation linear regression method was applied to calculate the cross-sections  
27 and spectral errors from a set of measurements recorded at a wide range of pressure to ensure  
28 optimal signal-to-noise ratio at all wavelengths. Based on this analysis, error bars on the  
29 measured cross-sections ranged between 3 and 10%. The overall features of measured cross-  
30 sections, such as peak positions of isotopologues, are consistent with previous studies. We  
31 provide improved spectral data for studying sulfur mass-independent fraction (S-MIF)  
32 signatures in  $\text{SO}_2$  photoexcitation. Our spectral measurements predict that  $\text{SO}_2$  photoexcitation  
33 produces  $^{33}E = -0.8 \pm 0.2\%$  and  $^{36}E = -4.0 \pm 0.4\%$ , whose magnitudes are smaller than those  
34 reported by Danielache et al. (2012).

35

## 36 1 Introduction

37 Sulfur dioxide ( $\text{SO}_2$ ) is the most common reduced sulfur compound present in many planetary  
38 atmospheres. This molecule has been known to exist in Earth, Venus, and Io for many years  
39 (Yung and DeMore, 1999). It has also been reported the presence of  $\text{SO}_2$  in the atmosphere of  
40 WASP-39b (Tsai et al., 2023). Understanding the photochemical properties of this molecule is  
41 essential for geochemical studies of planetary atmospheres. Its interactions with UV light  
42 trigger a cascade of chemical reactions that produce a variety of compounds, such as sulfuric  
43 acid ( $\text{H}_2\text{SO}_4$ ) or  $\text{S}_8$ , depending on the atmospheric redox state.

44 Stable isotopes are a powerful tool for studying and understanding a variety of geochemical  
45 processes. Such applications involve singly substituted isotopes, a combination of the same  
46 isotope with different masses which creates mass-dependent and mass-independent relations,  
47 and more than one isotope within the same molecule known as clumped isotopes (e.g., Eiler et  
48 al., 2014). The sulfur mass-independent fractionation (S-MIF) signatures (non-zero  $\Delta^{33}\text{S}$  and  
49  $\Delta^{36}\text{S}$  values) in the geological record have been shown to be non-zero before  $\sim 2.3\text{ Ga}$   
50 coinciding with the rise of oxygen levels in the atmosphere (Farquhar et al., 2000; Ono, 2017).  
51 Studies by Farquhar and co-workers (Farquhar et al., 2001; Masterson et al., 2011) and  
52 subsequent chemical chamber experiments (Endo et al., 2019; Endo et al., 2016) have shown  
53 that  $\text{SO}_2$  photodissociation and photoexcitation reactions under conditions free of oxygen  
54 produce large S-MIF signatures, although the previous experiments have not fully reproduced  
55 the Archean record such as relationships between  $\Delta^{33}\text{S}$  and  $\Delta^{36}\text{S}$  and between  $\delta^{34}\text{S}$  and  $\Delta^{33}\text{S}$   
56 (e.g., Ono, 2017; Endo et al., 2022b). An atmospheric photochemical model study by Pavlov  
57 and Kasting (2002) showed that SO radical produced during photolysis rapidly oxidized back  
58 to  $\text{SO}_2$  with  $10^{-5}$  of present atmospheric levels of  $\text{O}_2$  and therefore setting a maximum level of  
59 atmospheric oxygen abundance in which the S-MIF can be preserved, yet no model study has  
60 succeeded into reproducing the geological record. The work done to constrain the mechanisms  
61 and the atmospheric conditions that explain the S-MIF in the geological record is extensive and

62 a full summary is beyond the scope of this report (e.g., Ono, 2017; Thiemens and Lin, 2019)  
 63 but current understanding points to a combination of mechanisms including the photoexcitation  
 64  $\tilde{B}^1B_1$ - $\tilde{X}^1A_1$  band of the SO<sub>2</sub> molecule (Endo et al., 2016).

65 In the present earth, sulfur aerosols produced in the lower stratosphere from material uplifted  
 66 by plumes during Plinian eruptions and collected from Antarctic and Greenland ice cores show  
 67 an S-MIF signature distinct from Archean sulfides and sulfates (Baroni et al., 2007). Hattori et  
 68 al. (2013), based on the data reported by Danielache et al. (2012), reported that SO<sub>2</sub>  
 69 photoexcitation in the lower stratosphere produce signals compatible with the ice core record.  
 70 A subsequent study presented by Whitehill et al. (2013) showed that the fate of the photoexcited  
 71 fragment is not only direct oxidation by O<sub>2</sub>, as assumed in the Hattori et al. (2013) study, but  
 72 follows a branching mechanism due to quenching in which a fraction of the molecules in the  
 73  $\tilde{A}^1A_2/\tilde{B}^1B_1$  state are converted to the  $\tilde{a}^3B_1$  state. They further show an isotope selective spin-  
 74 orbit interaction between the singlet ( $\tilde{A}^1A_2/\tilde{B}^1B_1$ ) and triplet ( $\tilde{a}^3B_1$ ) manifolds. Despite the  
 75 extensive work done so far, further quantification of the isotopic effect during the  $\tilde{B}^1B_1$ -  
 76  $\tilde{X}^1A_1$  and  $\tilde{A}^1A_2$ - $\tilde{X}^1A_1$  excitation is needed.

77 The highly structured SO<sub>2</sub> UV absorption spectrum directly results from electronic transitions  
 78 and a complex and nuanced set of vibrational and rotational energy levels (Herzberg, 1945).  
 79 The single report on the <sup>32</sup>SO<sub>2</sub>, <sup>33</sup>SO<sub>2</sub>, <sup>34</sup>SO<sub>2</sub>, and <sup>36</sup>SO<sub>2</sub> (hereafter <sup>32,33,34,36</sup>SO<sub>2</sub>)  $\tilde{B}^1B_1$ -  
 80  $\tilde{X}^1A_1$  absorption spectrum from Danielache et al. (2012) has a spectral resolution of 8 cm<sup>-1</sup>  
 81 which is still far from fully resolved (Stark et al., 1999). Although from the  $\tilde{C}^1B_2$ - $\tilde{X}^1A_1$   
 82 absorption band, spectral measurements by Endo et al. (2015), SO<sub>2</sub> column density dependence  
 83 on cross-sections were observed (especially, this apparent column density and cross-sections  
 84 relation was stronger at absorption peaks; see Endo et al., 2015 Figure 1). Further analysis  
 85 suggested that insufficient spectral resolution relative to absorption line width explains this  
 86 phenomenon (Endo et al., 2015). The lack of resolution directly affects the peak separation and  
 87 further interferes with the accuracy of S-MIF calculations, which would significantly impact  
 88 the study of light-induced isotopic effects (See Endo et al., 2015 Figure S1). High-resolution  
 89 spectrum is therefore necessary for better understanding spectroscopic properties and  
 90 accurately the absorption spectra (Wu et al., 2000). Fully resolved spectra (Koplow et al., 1998)  
 91 with a low level of noise would be the authoritative yet near unachievable measurement for an  
 92 entire absorption band.

93 Recent studies by Lyons et al. (2018) have reported pressure room temperature broadening  
 94 coefficients of  $0.30 \pm 0.03$  cm<sup>-1</sup> atm<sup>-1</sup> and  $0.40 \pm 0.04$  cm<sup>-1</sup> atm<sup>-1</sup> for N<sub>2</sub> and CO<sub>2</sub> respectively  
 95 for the  $\tilde{C}^1 - \tilde{X}^1$  absorption band and Leonard (1989) reported broadening coefficients of  $0.237$   
 96  $\pm 0.0011$  cm<sup>-1</sup> atm<sup>-1</sup> and  $0.325 \pm 0.0015$  cm<sup>-1</sup> atm<sup>-1</sup> for N<sub>2</sub> and CO<sub>2</sub> respectively for the  $\tilde{B}^1 -$   
 97  $\tilde{X}^1$  absorption band. There are studies suggesting a largely congested line profile for the SO<sub>2</sub>  
 98 electronic spectra. The basis for such an assertion are from theoretical calculations of the  
 99 bound-type excited electronic states coupled to rotational-vibrational transitions (Kumar et al.,  
 100 2015). Models reported by Lyons et al. (2018) used a line spacing of 0.25 cm<sup>-1</sup> for the  $\tilde{C}^1 - \tilde{X}^1$   
 101 band which is not the absorption band concerned in this report, but it might show a similar  
 102 behavior. A quantitative assessment of natural widths and line congestion at different spectral  
 103 regions is yet to be reported. The computational requirement for a theoretical calculation of a  
 104 high  $J$  electronic spectrum is a challenge to be reckoned with. Reports on  $J$  and  $K$  values ( $J$  and

105  $K$  stand for rotational and vibrational wavefunction, not to be confused with the integrated  
106 photo-dissociation rate constant  $J$ ) such as the reported by Kumar et al. (2015) for total angular  
107 momentum  $J = 0-10$  are illustrative of the amount of computations needed for a full spectrum  
108 calculated at high  $J$ . Pressure broadening coefficients put together with the above suggested  
109 line density of these systems will cause line profile overlap and thus creating a pseudo-  
110 broadened spectra or sections of the most congested parts of the rovibrational progression and  
111 thus reducing the minimal requirement of spectral resolution for meaningful photo-induced  
112 isotopic effects. In summary, a combination of spectral resolution, pressure broadening, and  
113 profile overlap suggests that the data in this report might be suitable for the study of isotopic  
114 effects happening in a planetary atmosphere with a total atmospheric pressure close to 1 atm.  
115 An additional known issue is that even if a fully resolved spectrum is achieved, it is difficult  
116 to obtain high precision with high-resolution measurements because the noise increases at high-  
117 resolution measurements (see comparison in Table 1). The issue would lead to large errors of  
118 calculated photodissociation rate constants and associated isotopic effects. In order to address  
119 this issue we have implemented a linear regression method that has been widely used in Fourier  
120 transform spectroscopy to reduce noise and increase spectral precision (Barra et al., 2021;  
121 Dreissig et al., 2009; Meyer-Jacob et al., 2014; Santos et al., 2021).  
122 In this study, an experimental setup of a Fourier transform spectrometer (VERTEX 80v, Bruker,  
123 Japan) was optimized to adapt measurements in the UV band. We used the least absolute  
124 deviation (LAD) linear regression for data calibration and measured the  $^{32}\text{SO}_2$ ,  $^{33}\text{SO}_2$ ,  $^{34}\text{SO}_2$ ,  
125 and  $^{36}\text{SO}_2$ ,  $\tilde{B}^1B_1-\tilde{X}^1A_1$  absorption spectrum ranges from 240 to 320 nm with a resolution of  
126  $0.4\text{ cm}^{-1}$  and 3–10% of error.

## 127 2 Experimental

### 128 2.1 $\text{SO}_2$ isotopologues samples

129 The isotopically enriched  $^{32,33,34,36}\text{SO}_2$  gas samples were prepared from elemental  $^{32}\text{S}$ ,  $^{33}\text{S}$ ,  $^{34}\text{S}$ ,  
130 and  $^{36}\text{S}$  powder (Isoflex USA) sealed with CuO in quartz tubes under vacuum, heated at  $950^\circ\text{C}$   
131 for 15 min. Separation of  $\text{SO}_2$  samples and unreacted  $\text{O}_2$  was done by freeze-pump-thaw  
132 cycling. The components of the gas phase labeled samples were confirmed and purified using  
133 a GC-MS, and the products purity was checked by quantitative IR spectroscopy (Danielache et  
134 al., 2012). Details of sample preservation are described in Endo et al. (2022a).

### 135 2.2 Instrument setups

136 The gas cell and inlet gas system follows Endo et al. (2022a). The UV absorption cross-sections  
137 were determined using a Fourier transform spectrometer (VERTEX 80v, Bruker, Japan) with  
138 an external deuterium lamp (L6301-50, Hamamatsu, Japan) equipped at the inlet port on the  
139 right spectrometer side. Two capacitance manometers (CMR362 and CMR364, Pfeiffer,  
140 Germany) calibrated the pressure using a full-range gauge (PGE500, INFICON, Germany) and  
141 local weather reports. An oil pump was added to the gas line system for pre-vacuuming to  
142 extend the lifetime of the turbopump system (Pfeiffer, Germany).

143 Signal drifting from the light source was observed, where the signal intensity decreases over  
144 time. Following a commonly used method (Danielache et al., 2008; Danielache et al., 2012;

145 Endo et al., 2022a; Vandaele et al., 2009), where the background signal intensity at the time of  
 146 the sample signal measurement was derived by alternating the background and sample signal  
 147 measurements and calculating the average of the two background signal before and after each  
 148 sample signal measurement.

149 Numerous measurement parameters were adjusted to balance high-resolution and relatively  
 150 low noise levels while limiting the measurement time to avoid excessive errors brought by  
 151 signal drift. The interferogram from a single measurement was derived from an average of 150  
 152 scans at a resolution of  $0.4 \text{ cm}^{-1}$  using single-sided and bi-directional acquisition mode and  
 153 was converted to signal intensity spectrum by Fourier transform using boxcar apodization  
 154 function and Mertz phase correction mode to preserve the most original data possible. A  
 155 frequency window from 0 to  $60,000 \text{ cm}^{-1}$  and a zero-filling number of 2 produced a spectrum  
 156 ranging from  $41666$  to  $29400 \text{ cm}^{-1}$  with a data point spacing of ca.  $0.12055 \text{ cm}^{-1}$ . No prominent  
 157 peaks spread due to the grazing-incidence light in the UV region measurement was observed,  
 158 and an 8 mm aperture size was selected. The VERTEX 80v instrument used in our  
 159 measurements is capable of a maximum spectral resolution of  $0.1 \text{ cm}^{-1}$ . However, the optimal  
 160 trade-off between spectral resolution and spectral noise was found to be  $0.4 \text{ cm}^{-1}$  which is  
 161 between 5 to 10 times lower in resolving power than the suggested optimal spectral resolution  
 162 (Rufus et al., 2003).

### 163 2.3 Measurements

164 The Beer-Lambert law,

$$165 \quad A = \ln \frac{I_0}{I} = \ln \frac{1}{Trans} = \sigma l \rho \quad (1)$$

166 Shows that absorbance  $A$  is proportional to attenuating number density of the gas sample  $\rho$  (in  
 167 this report approximated as gas pressure, assuming a constant temperature). The radiant power  
 168 intensity is reduced from  $I_0$  to  $I$ ,  $Trans$  is the transmittance,  $\sigma$  is the absorption cross-sections,  
 169 and  $l$  is the optical path length. Both logarithm and natural logarithm definition formats of  
 170 absorbance are widely used. Which format is used does not affect the  $A \propto C$  relationship, we  
 171 used the natural logarithm format for a more convenient calculation of cross-sections. In this  
 172 report,  $\text{SO}_2$  absorption cross-section ( $\sigma$ ) at each wavelength ( $\lambda$ ) was calculated through the  
 173 application of the Beer-Lambert law,

$$174 \quad \sigma(\lambda) = -\frac{RT}{PN_A z} \ln \frac{2I(\lambda)}{I_{0a}(\lambda) + I_{0b}(\lambda)} = -\frac{1}{\rho z} \ln \frac{I(\lambda)}{I_{0ave}(\lambda)} = -\frac{1}{\rho z} \ln Trans(\lambda) \quad (2)$$

175 Where  $R$  is the gas constant,  $T$  is the room temperature in the laboratory,  $P$  is the sample  
 176 pressure during measurement,  $N_A$  is the Avogadro number,  $z$  is the sample cell length (10.0  
 177 cm) through which the light passes,  $I$  is the measured sample signal intensity,  $I_{0a}$  and  $I_{0b}$  are  
 178 the measured background signal intensity before and after a single sample measurement as  
 179 mentioned above, and  $I_{0ave}$  is the mean signal intensity of  $I_{0a}$  and  $I_{0b}$ , Substituting (1) into  
 180 (2) yields the following,

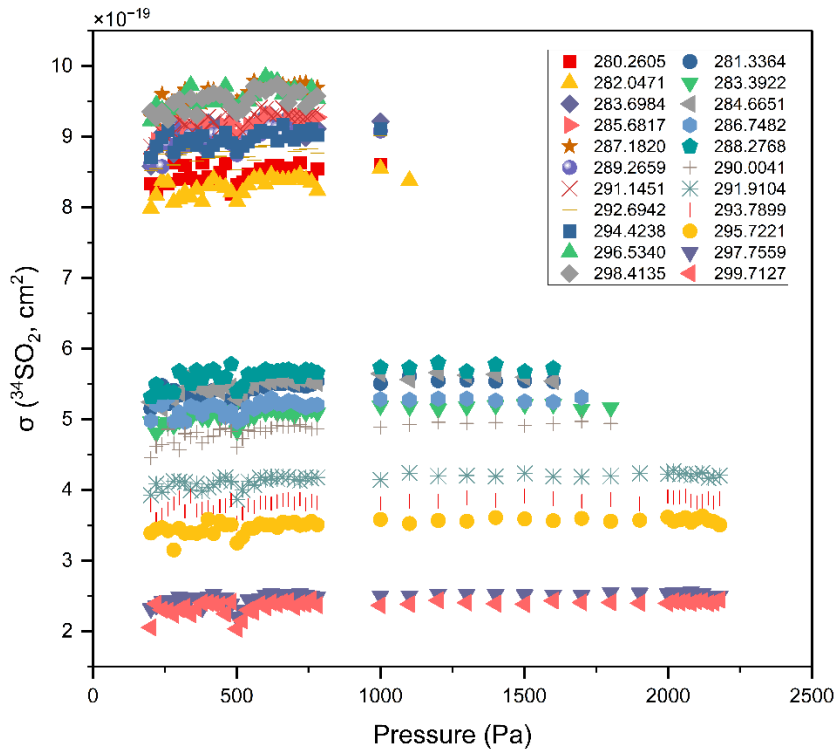
$$181 \quad \sigma(\lambda) = -\frac{RT}{PN_{AZ}} \ln T(\lambda) = k_1 \cdot \frac{A(\lambda)}{P} \quad (3)$$

182 Where  $k_1 = \frac{RT}{N_{AZ}}$ , and

$$183 \quad \sigma(\lambda) = -\frac{RT}{PN_{AZ}} \ln T(\lambda) = k_2 \cdot TA(\lambda) \quad (4)$$

184 Where  $k_2 = \frac{R}{PN_{AZ}}$ .

185 Equations (3) and (4) indicate that when  $\sigma$  is either pressure or temperature dependent, the  
 186 linear relationship between  $A$  and  $P$  is not valid. In this study, the temperature is assumed to be  
 187 constant since variability was within a range of a few digress. The measured data showed no  
 188 pressure-dependent cross-sections. **Figure 1** shows the relation between sample pressure in the  
 189 gas cell and measured absorption-cross sections. Previous absorption cross-section  
 190 measurements of various gas and liquid species have acknowledged deviations from the Beer-  
 191 Lambert law, that is an apparent cross-section pressure dependency (e.g., Kostkowski and Bass,  
 192 1956; Anderson and Griffiths, 1975; Mellqvist and Rosén, 1996; Endo et al., 2015; Li et al.,  
 193 2022). In both reports the origin of such non-linear behavior is attributed to low spectral  
 194 resolution of the instrument. The data presented in this report, which was recorded at spectral  
 195 resolution of  $0.4 \text{ cm}^{-1}$ , shows no apparent pressure-dependent cross-section variability (**Figure**  
 196 **1**). Thus, it is not required to correct the apparent cross-section pressure dependency.



198 **Figure 1:** Individual cross-section data of each peak and valley at different pressures from  
 199 280–300 nm for  $^{34}\text{SO}_2$ . The  $^{34}\text{SO}_2$  pressure ranges from 200–2200 Pa. No apparent pressure-  
 200 dependent cross-section phenomenon was observed.

201

202 In actual measurements, many sources of uncertainty can affect the linear relationship between  
 203  $A$  and  $P$ . In the case of a high-precision Fourier transform spectrometer, the dark current and  
 204 amplifier noise from regions where source intensity and detector sensitivity are low, the photon  
 205 detector shot noise, the cell positioning uncertainties, etc., making different orders of impact  
 206 on the relative signal intensity uncertainty (Skoog et al., 2017). These random noises are almost  
 207 impossible to distinguish from each other thoroughly. Common solutions include averaging  
 208 multiple sets of measurements (Blackie et al., 2011; Rufus et al., 2003; Stark et al., 1999;  
 209 Vandaele et al., 2009), adding weights to the parameters that characterize the data (Danielache  
 210 et al., 2008; Danielache et al., 2012), and calibration of  $\text{SO}_2$  column density dependence on  
 211 measured cross-sections with a least squares method (Endo et al., 2015). Nonetheless,  
 212 conventional methods still do not resolve the bias that noise from different sources introduce  
 213 to the actual absorptivity.

214 In this study, we implemented a linear regression technique to rule out the effect of random  
 215 noise. The LAD method was deployed to clarify the linear relationship between  $A$  and  $P$ ,  
 216 following the purpose of minimizing the sum of the absolute values of the residuals  $S$  between  
 217 raw data  $y_i$  to the fitted data  $f(x_i)$ ,

$$218 \quad \operatorname{argmin} S = \sum_{i=1}^n |y_i - f(x_i)| \quad (5)$$

219 A universal algorithm from the Scikit-Learn machine learning library (Pedregosa et al., 2011)  
 220 for the Python programming language was used for computational efficiency considerations.  
 221 Based on the degree of data dispersion, scenarios that linear regression needs to target can be  
 222 categorized into three. Case 1: Little effect of random noise on the data, where  $A$  and  $P$  have  
 223 good linear fit, and there is little difference compared to the commonly used least squares (LS)  
 224 linear regression. Case 2: The effect of random noise on individual data creates outliers, and  
 225 the LAD method excludes the impact from outliers much better than the LS method. Case 3:  
 226 Highly discrete data in high noise regions, the linear relationship between  $A$  and  $P$  is almost  
 227 indistinguishable, and all current methods do not guarantee noise removal.

228 The number of valid measurements at a given wavelength used in the LAD linear regression  
 229 ranged between 10 and 70 depending on signal-to-noise and the amount of available sample  
 230 (**Figure S2**). The increased number of measurements are a necessary condition for reducing  
 231 the errors associated with signal-to-noise issues. Previous measurements on isotopic effects of  
 232 ultraviolet absorption cross sections reported by the authors (Danielache et al., 2008, 2012;  
 233 Hattori et al., 2011; Endo et al., 2015, 2022a) have been aware of this issue but limitations on  
 234 sample and instrument accessibility have limited the number of measurements. In this report  
 235 the number of measurements were increased to a number where an analysis of the limit of noise  
 236 reduction by number of measurements was conducted. At least 10 measurements are required

237 to reduce the LAD algorithm error. 15–25 sets of measurements are recommended, and the  
 238 improvement in error is no longer apparent after more than 30 sets.

239 With the above reference parameters, the final cross-sections are calculated as follows. Firstly,  
 240 the collected raw data were prefiltered to retain the data with transmittance from 0.1 to 0.95,  
 241 which not only excluded the data with too low signal intensity but also the transmittance range  
 242 was chosen to consider the effect of instrument noise on the measurement precision (Skoog et  
 243 al., 2017). Next, data with signal-to-noise ratio (SNR) less than 20 were excluded to further  
 244 improve data quality. The filtered data are involved in the following data correction of the  
 245 linear relationship between  $A$  and  $P$  by the LAD method. Finally, the corrected  $A$  allows the  
 246 calculation of the cross-sections at the corresponding wavelength.

## 247 2.4 Error budgets

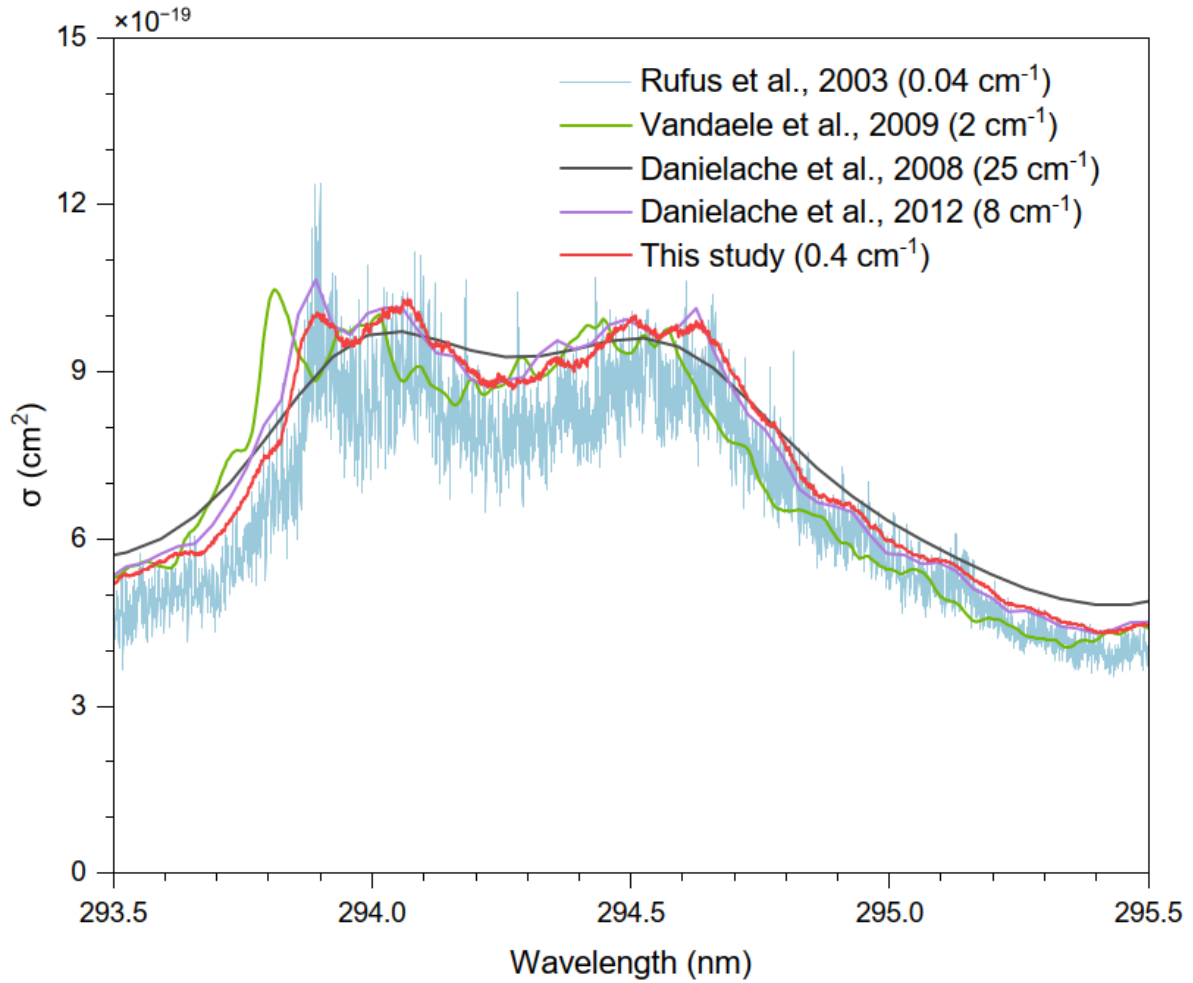
248 The errors in this study came mainly from four main sources. (1) The temperature variation of  
 249 the experimental environment was within 2.5 K, introducing an error of 0.85% to the final  
 250 cross-sections. (2) The mechanical error of the pressure gauge, according to the manufacturer's  
 251 instructions, has a validity of about 0.2%. (3) Each measurement took about 20 min, and the  
 252 pressure change due to SO<sub>2</sub> adsorption to the sample cell and stainless tube wall introduced an  
 253 error of about 0.2%. (4) The errors from instrumental random noises are mostly reflected in the  
 254 dispersion of the linear relationship between  $A$  and  $P$ , following,

$$255 \quad S_{y/x} = \sqrt{\frac{\sum (y_i - f(x_i))^2}{n - 2}} \quad (6)$$

## 256 3 Results and discussions

### 257 3.1 Comparisons with previous studies

258 The measured <sup>32</sup>SO<sub>2</sub> absorption spectrum in the present study is compared to four previous  
 259 studies on SO<sub>2</sub> in the  $\tilde{B}^1B_1 - \tilde{X}^1A_1$  absorption band (**Figure 2**) and spectral summary listed in  
 260 **Table 1**. There are two previous studies about the SO<sub>2</sub> isotopologues with spectral resolution  
 261 of 25 cm<sup>-1</sup> (Danielache et al., 2008) and 8 cm<sup>-1</sup> (Danielache et al., 2012) and errors of 1.2–2.5%  
 262 and 1.2–8.2% respectively. For comparison, two naturally abundant SO<sub>2</sub> studies with high  
 263 resolution are presented. The study from Vandaele et al. (2009) with spectral resolution of 2  
 264 cm<sup>-1</sup> and 4–6% error. A high-resolution natural abundance measurement from Rufus et al.  
 265 (2003) with spectral resolution of 0.04–0.13 cm<sup>-1</sup> resolution and 5% error. This study improves  
 266 the spectral resolution of the existing isotopic spectrum by a factor of 20, while the error in the  
 267 260–300 nm band is comparable to spectra of natural abundance at about ten times higher  
 268 resolution.



269

270 **Figure 2:** Comparison of measured  $^{32}\text{SO}_2$  absorption spectrum in this study with spectra  
 271 reported by Rufus et al. (2003), Vandaele et al. (2009), Danielache et al. (2008) ( $^{32}\text{SO}_2$ , 25  
 272  $\text{cm}^{-1}$ ), and Danielache et al. (2012) at the 293.5–295.5 nm spectral range. All the reported  
 273 spectra were measured at room temperature (293–298 K) therefore spectral differences are not  
 274 expected to be produced by temperature differences. Spectra reported by Rufus et al. (2003),  
 275 Vandaele et al. (2009) are for natural abundance  $\text{SO}_2$  samples.  $^{32}\text{SO}_2$  spectrum data in  
 276 Danielache et al. (2008) used natural abundance samples and calibrated with measured  $^{33}\text{SO}_2$   
 277 and  $^{34}\text{SO}_2$  spectra. Spectra in this report and Danielache et al., (2008) are from isotopically  
 278 enriched  $^{32}\text{SO}_2$  samples.

279

280 **Table 1:** Summary and comparison of studies on  $\text{SO}_2$  absorption b-band.

Reference	Isotope	Resolution ( $\text{cm}^{-1}$ )	Average Error (%)	Temperature (K)
Present study	$^{32,33,34,36}\text{S}$	0.4	~5.1( $^{32}\text{SO}_2$ ) ~4.0( $^{33}\text{SO}_2$ ) ~4.5( $^{34}\text{SO}_2$ ) ~4.1( $^{36}\text{SO}_2$ )	293

Rufus et al. (2003)	Natural abundance	0.04-0.13	~5	295
Vandaele et al. (2009)	Natural abundance	2	~4-6	298
Danielache et al. (2012)	<sup>32,33,34,36</sup> S	8	~2.2( <sup>32</sup> SO <sub>2</sub> ) ~1.8( <sup>33</sup> SO <sub>2</sub> ) ~1.2( <sup>34</sup> SO <sub>2</sub> ) ~2.5( <sup>36</sup> SO <sub>2</sub> )	293
Danielache et al. (2008)	Nat., <sup>33,34</sup> S	25	~1.2(Nat.) ~3.8( <sup>33</sup> SO <sub>2</sub> ) ~8.2( <sup>34</sup> SO <sub>2</sub> )	293

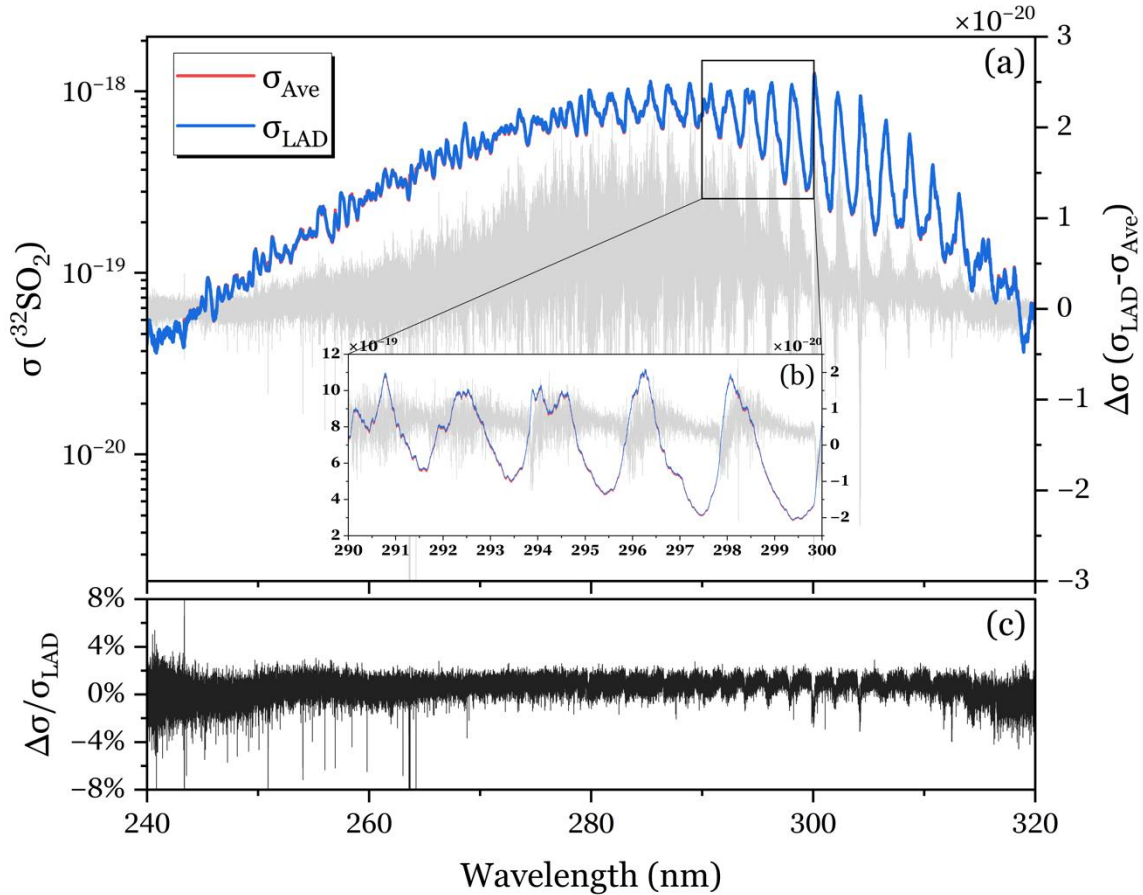
281 *Note.* Comparison of peaks at different resolutions show that the spectrum in this study exhibits  
 282 significantly better peak separation than the low-resolution studies (Danielache et al., 2008;  
 283 Danielache et al., 2012; Vandaele et al., 2009). Even the spectrum from Vandaele et al. (2009),  
 284 which has only a five-times difference in resolution, can observe much more resolved peaks.  
 285 This study also shows excellent control of baseline noise, which is about the same as the lower  
 286 resolution spectrums compared to the ten times higher resolution spectrum from Rufus et al.  
 287 (2003). The peak position in this study fits the result from Danielache et al. (2012), while the  
 288 spectrum from Danielache et al. (2008) is unsuitable for comparison due to band shape  
 289 distortion by low resolution. The peak position in the spectrum from Vandaele et al. (2009)  
 290 shows a slightly blue shift compared to the spectrum from Rufus et al. (2003), which is also of  
 291 natural abundance.

292 The cross-sections calculated using the LAD method are also compared to those calculated  
 293 using the averaging method as illustrated in **Figure 3**. The new LAD method perfectly  
 294 reproduces the peak positions and peak intensities derived from the averaging method over the  
 295 entire measurement band. From **Figure 3 (b)**, it can be concluded that the subtle differences  
 296 between the two methods are mainly reflected in the position of the spectral peaks, and the  
 297 magnitude of the difference increases with the intensity of the peaks. **Figure 3 (c)** shows that  
 298 the difference is about  $10^{-2}$  of the intensity of the cross-sections, and there is a relatively high  
 299 difference of about 2-3% at the low SNR positions at both ends of the measurement band, and  
 300 about 1% at the high SNR positions in the middle of the measurement band. The comparison  
 301 of errors between two methods are shown in **Figure 4**, where the spectral data of <sup>32</sup>SO<sub>2</sub>  
 302 measured in this study are used. The error calculation of averaging method follows Stark et al.  
 303 (1999) that includes uncertainty in the absorbing column density  $N$  of SO<sub>2</sub>, uncertainties in the  
 304 values of  $I(\lambda)$  and  $I_{ave}(\lambda)$  associated with the measurement SNR for  $I_{0ave}(\lambda)$ , and the  
 305 systematic errors associated with inadequate spectral resolution, following,

$$306 \quad \frac{\Delta\sigma}{\sigma} = \left[ \left( \frac{\Delta N}{N} \right)^2 + \left( \frac{1}{(SNR)N\sigma} \right)^2 \{1 + e^{2N\sigma}\} \right]^{0.5} \quad (7)$$

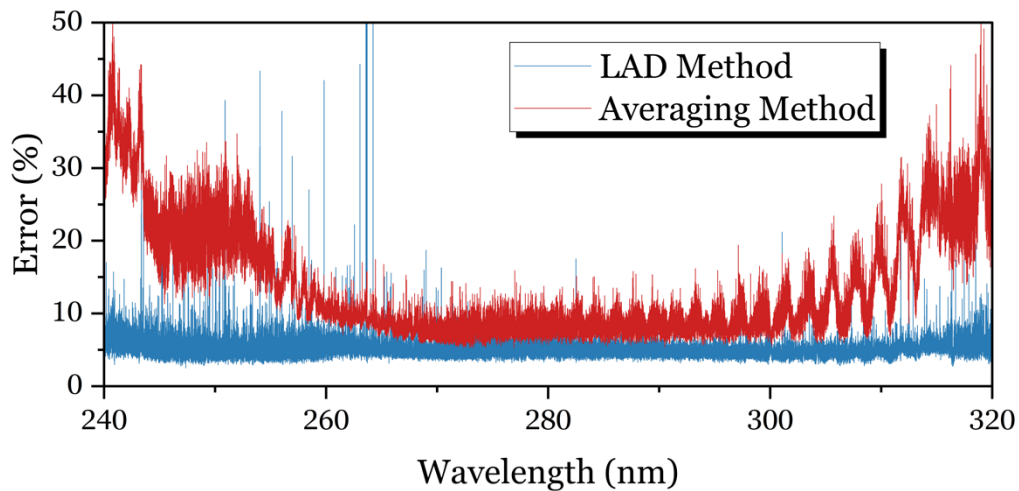
307 The averaging method shows higher error than the LAD method, with 20-40% error in low  
 308 SNR regions at both ends of the measurement band range and 10% in high SNR regions. The  
 309 mean error for the averaging method is 15.1% in the 240-320 nm band range, compared with  
 310 the 5.1% error using the LAD method, indicating the new algorithm reduces the error by a  
 311 factor of about three. Since the LAD method does not require separating multiple sources of

312 noise and calculating the errors brought by each type of noise individually, it treats them as a  
 313 whole and discriminates the errors by the dispersion of the linear relationship between  
 314 absorbance and gas pressure, as well as introducing a sufficiently large number of measurement  
 315 groups to improve the reliability of the data.



316

317 **Figure 3:** Comparison of spectra obtained the LAD and averaging methods (panel a), and  
 318 difference between both methods grey color line for the 240–320 nm spectral range. Panel (b)  
 319 shows an enlarged comparison for the 290–300 nm spectral range. Panel (c) shows the relative  
 320 of difference between the two methods respect to the spectrum obtained by the LAD method.  
 321 From the panel c can be seen that both methods yield spectra with a maximum difference of  
 322 c.a.  $\pm 4\%$ .



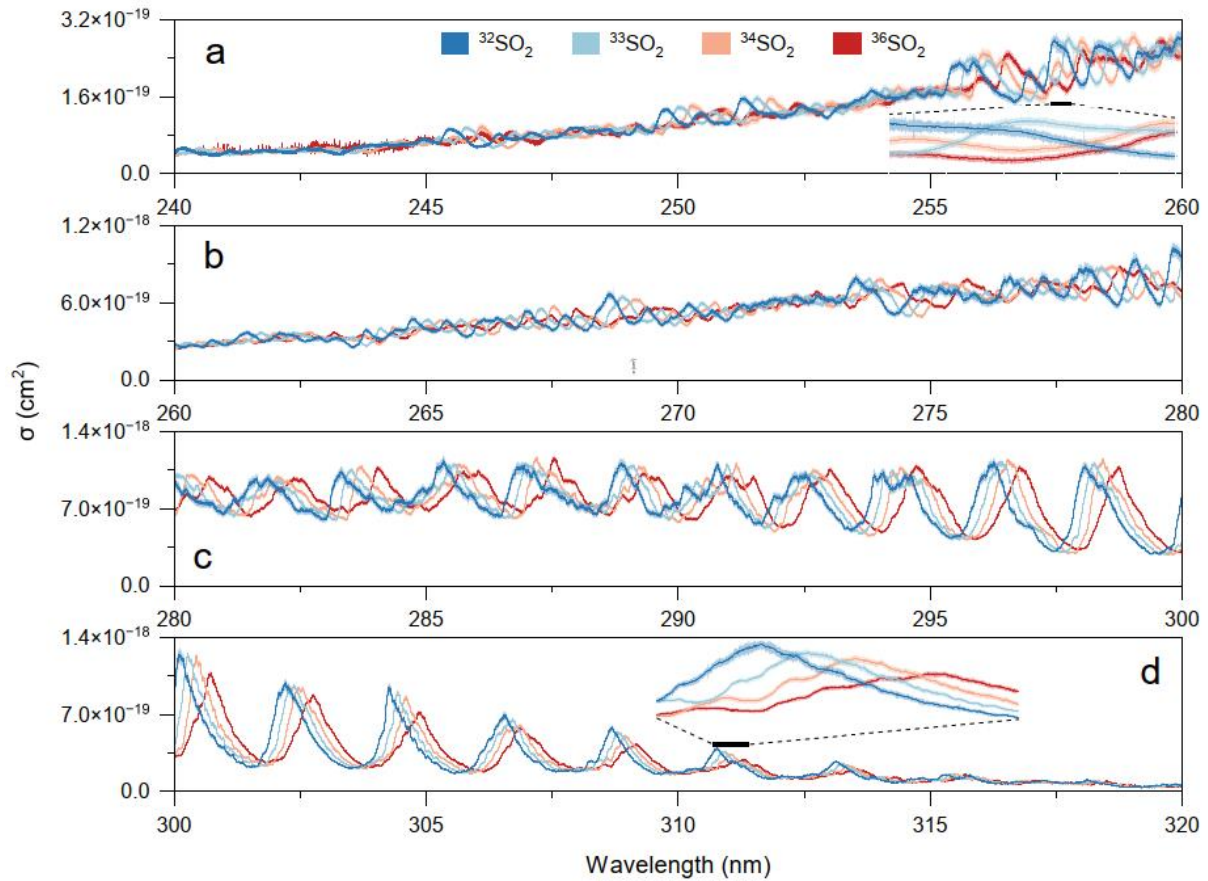
323

324 **Figure 4:** Error comparison between the LAD method and the averaging method for the  
 325 spectral data of  $^{32}\text{SO}_2$  measured in this study. The error calculation of the averaging method  
 326 follows Stark et al. (1999) that includes the uncertainty in the column density, the uncertainties  
 327 in the value of  $I(\lambda)$  and  $I_{0ave}(\lambda)$  associated with the measurement SNR for  $I_{0ave}(\lambda)$ , and the  
 328 systematic errors associated with inadequate spectral resolution.

329

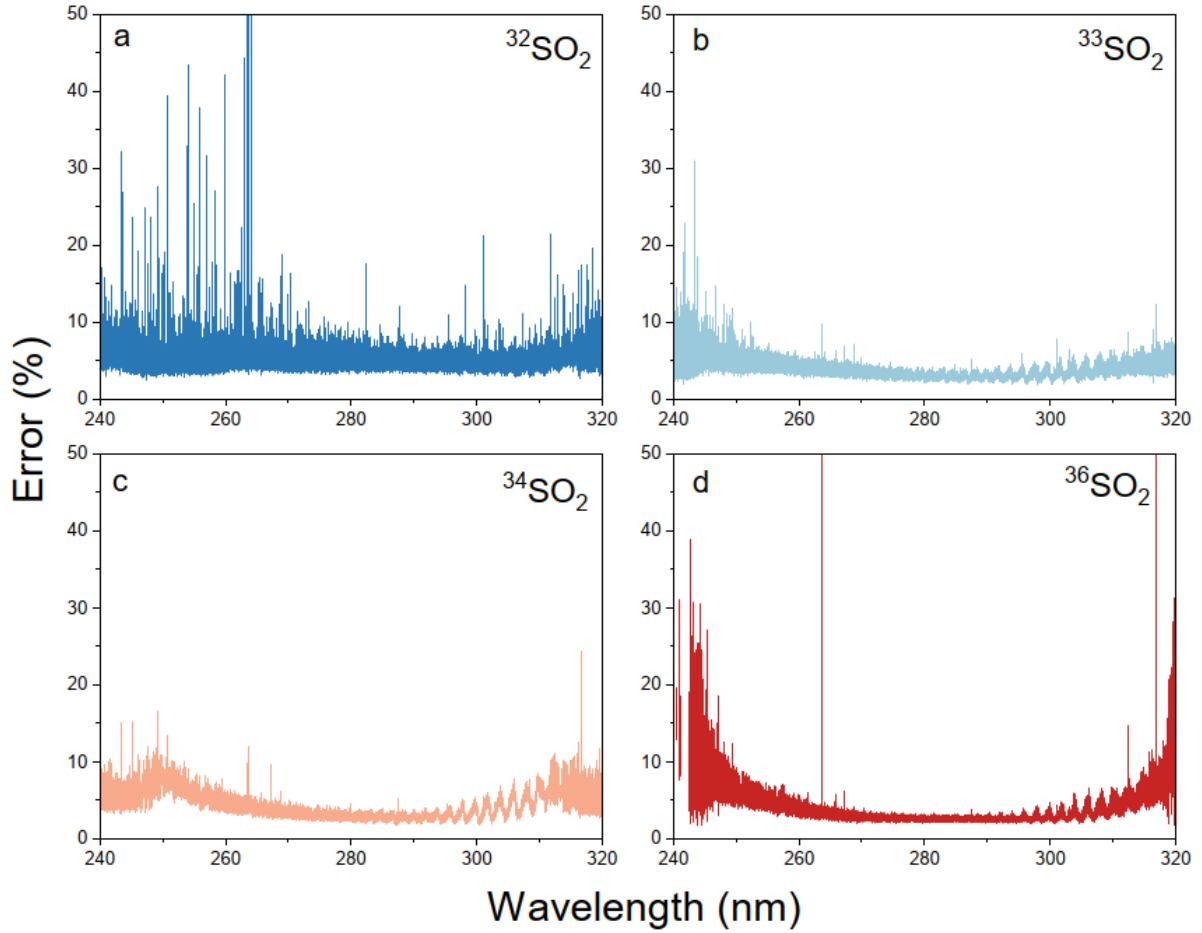
### 330 3.2 Isotopic Fractionation in $\text{SO}_2$ Photoexcitation

331 The measured absorption cross-sections are shown in **Figure 5**, where values of  $\sigma$  for  
 332  $^{32,33,34}\text{SO}_2$  at 240–320 nm were successfully measured. However, due to insufficient samples  
 333 as illustrated in **Figure S3**,  $^{36}\text{SO}_2$  in the 240–245 nm band could not be measured. The errors  
 334 in the measured cross-sections are in the range of 3–10% shown in **Figure 6**, with relatively  
 335 high errors in the 240–260 nm and 310–320 nm bands.



336

337 **Figure 5:** Measured absorption cross-sections of  $^{32}\text{SO}_2$ ,  $^{33}\text{SO}_2$ ,  $^{34}\text{SO}_2$ , and  $^{36}\text{SO}_2$ , absorption  
 338 cross-sections and estimated errors. For clarity panels a,b,c and d divide the spectrum in four  
 339 spectral ranges 240–260nm, 260–280 nm, 280–300 nm and 300–320 nm respectively. Sub-  
 340 sets in panels a and d show an expanded fraction of the spectra to make more readable the  
 341 associated error bars to each wavelength. As the mass of the 13 isotopologues increases a  
 342 significant redshift in the position of the peak of the absorption spectrum can be observed  
 343 starting at the spectral band origin near 317 nm.



344

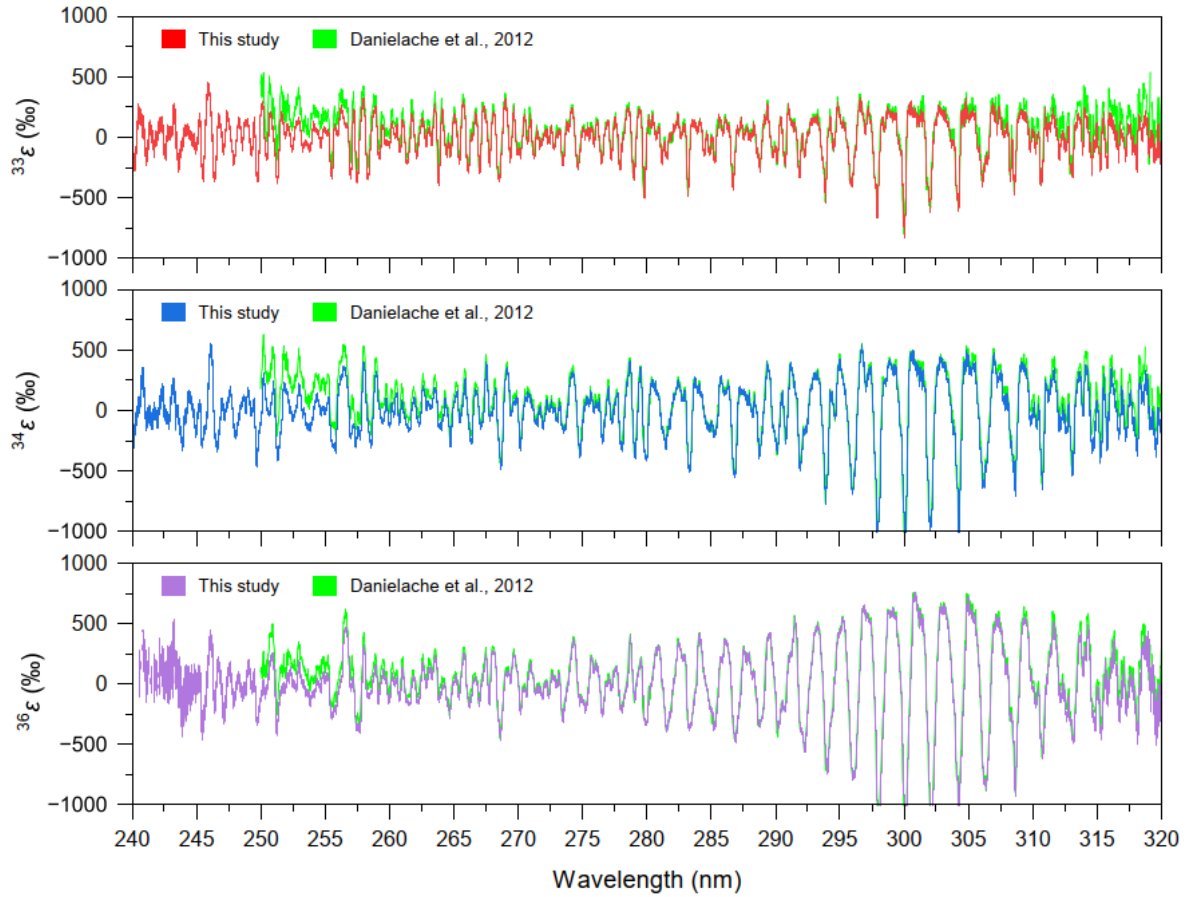
345 **Figure 6:** Relative error of  $^{32}\text{SO}_2$ ,  $^{33}\text{SO}_2$ ,  $^{34}\text{SO}_2$ , and  $^{36}\text{SO}_2$  respect to measured absorption  
 346 cross-sections. Lack of precision due to insufficient signal-to-noise ratio is more pronounced  
 347 at edges of the measurement spectral band.

348

349 The redshift of the  $\text{SO}_2$  rare isotopologues relative to  $^{32}\text{SO}_2$  at each peak position is more  
 350 pronounced for heavier isotopes. The wavelength-dependent isotopic fractionation constant  
 351  $^{3x}\varepsilon(\lambda)$  was calculated to describe the isotopic effect (Ueno et al., 2009), following,

$$352 \quad ^{3x}\varepsilon(\lambda) = 1000 \times \ln \left[ \frac{\sigma^{3x}\text{SO}_2(\lambda)}{\sigma^{32}\text{SO}_2(\lambda)} \right] [\text{‰}] \quad (8)$$

353 where  $\sigma^{3x}(\lambda)$  is the absorption cross-section for a given isotopologue ( $^{3x}\text{S}$ , namely  $^{32}\text{S}$ ,  $^{33}\text{S}$ ,  
 354  $^{34}\text{S}$ , or  $^{36}\text{S}$ ) at wavelength  $\lambda$ . The result is shown in **Figure 7**, this study extends the existing  
 355 value of fractionation constant by 10 nm at shorter wavelengths compared to the previous study  
 356 (Danielache et al., 2012). The peak positions in the highly structured absorption cross-sections  
 357 are consistent with Danielache et al. (2012), but the values at both ends of the measurement  
 358 band are slightly smaller.



359

360 **Figure 7:** Fractionation constant of  $^{33,34,36}\epsilon$  as a function of wavelength from measured  
 361 absorption cross-sections ( $^{3x}\epsilon(\lambda)$ ) compared to the previous study (Danielache et al., 2012).  
 362 Newly reported spectra show a large wavelength specific isotopic effect which are similar to  
 363 previously reported spectra. Significant differences can be seen at edges of the measured  
 364 spectra in the  $\sim 250$  nm and  $\sim 315$  nm region.

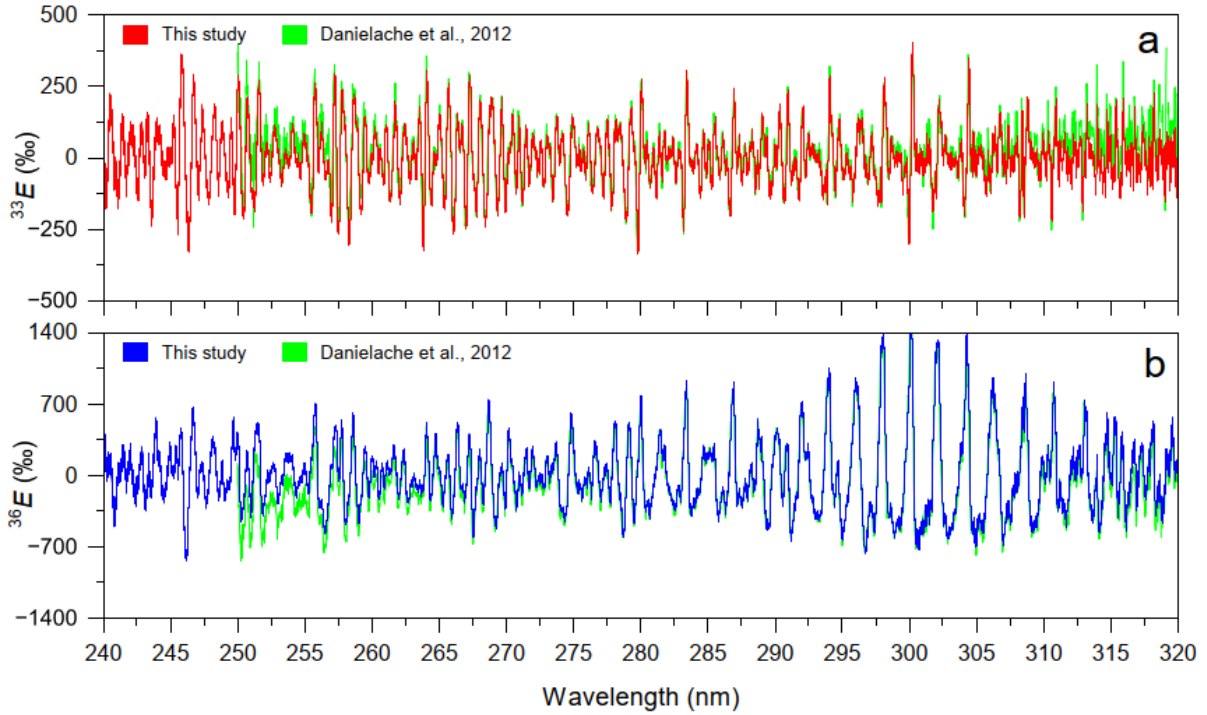
365

366 The magnitudes of S-MIF for the four stable sulfur isotopologues are given by the linear  
 367 expressions as follows,

$$368 \quad {}^{33}E_{\lambda} = {}^{33}\epsilon_{\lambda} - 0.515 \times {}^{34}\epsilon_{\lambda} \quad (9)$$

$$369 \quad {}^{36}E_{\lambda} = {}^{33}\epsilon_{\lambda} - 1.9 \times {}^{34}\epsilon_{\lambda} \quad (10)$$

370 where the values 0.515 and 1.9 are the high-temperature limit values for the equilibrium  
 371 partition function ratio for isotope exchange reactions (Hulston and Thode, 1965). As shown  
 372 in **Figure 8**, the S-MIF constant of  $^{33}E$  and  $^{36}E$  largely agree to the previous study (Danielache  
 373 et al., 2012), with the values at both ends of the measurement band are slightly deviated.



374

375 **Figure 8:** The Mass-independent fractionation constant  $^{33}E$  and  $^{36}E$  calculated from standard  
 376 S-MIF values of 0.515 and 1.9 as a function of wavelength compared to Danielache et al.  
 377 (2012). Newly reported spectra show a large wavelength specific isotopic effect which are  
 378 similar to previously reported spectra. Significant differences can be seen at edges of the  
 379 measured spectra in the  $\sim 250$  nm and  $\sim 315$  nm region.

380

381 Generally,  $^{33,34,36}\epsilon$  and  $^{33,36}E$  mostly reproduced the results from the previous study  
 382 (Danielache et al., 2012) regardless of the higher resolution of this report. The deviation at both  
 383 ends of the measurement band could come from many factors, the largest of which is likely to  
 384 be the low SNR brought about by insufficient background signal intensity.

385 The sulfur isotopic fractionation for  $\text{SO}_2$  photodissociation in  $\tilde{C}^1B_2-\tilde{X}^1A_1$  absorption band and  
 386 photoexcitation in  $\tilde{B}^1B_1-\tilde{X}^1A_1$  absorption band were also calculated. The photochemistry  
 387 reaction rates for each sulfur 16sotopologues in the atmosphere follows,

388 
$$^{3x}J = \int_{\lambda_0}^{\lambda_1} \Phi(\lambda) \cdot I(\lambda) \cdot ^{3x}\sigma(\lambda) d\lambda \quad (11)$$

389 Where  $\Phi$  is the quantum yield (assumed as 1) and  $I$  is the actinic solar flux derived from  
 390 Gueymard (2004). The S-MIF signatures  $^{33,36}E$  of sulfur isotopes by  $\text{SO}_2$  photochemical  
 391 reactions are then calculated from  $^{3x}J$  follow,

392 
$$^{3x}\epsilon = 1000 \ln \frac{^{3x}J}{^{32}J} [\text{‰}] \quad (12)$$

$$393 \quad {}^{33}E = {}^{33}\varepsilon - 0.515 \times {}^{34}\varepsilon \quad (13)$$

$$394 \quad {}^{36}E = {}^{36}\varepsilon - 1.9 \times {}^{34}\varepsilon \quad (14)$$

395 The errors derived from the LAD method produce a simple standard deviation which in this  
 396 report is represented as  $\sigma$  ( $\sigma^{3x}J$ ,  $\sigma^{3x}\varepsilon$  and  $\sigma^{3x}E$ ). For a detailed description on the error  
 397 propagation procedure see the corresponding section in the additional information. Calculated  
 398  ${}^{3x}J$  values from cross-sections obtained by the LAD and averaging methods are presented and  
 399 compared in **Figure 9** and **Table 2**. As presented in **Figure 2a**, cross-sections obtained by both  
 400 methods are almost identical and therefore the calculated  ${}^{3x}J$  values are numerically similar.  
 401 The propagated errors are significantly different where the robustness of the LAD method is  
 402 reflected in the propagated  $\sigma^{3x}J$  values which are roughly 2 orders of magnitude smaller to  
 403 those obtained by the averaging method. The reduction of the calculated  $\sigma^{3x}J$  values represent  
 404 a breakthrough since they do not overlap with each other (**Figure 9** red and blue data sets)  
 405 while the averaging method show significant overlap making the derived  $\sigma^{3x}\varepsilon$  and  $\sigma^{3x}E$   
 406 unreliable for geochemical predictions. The source in propagated error values can be traced to  
 407 random errors produced by noise in the measured signal intensity ( $I$  or  $I_0$  in Equation 1). Noise  
 408 in the measured signal intensity  $I$  or  $I_0$  for single measurements falls into the category of random  
 409 errors. However, repeated measurements (See Figure S3 for the number reliable measurements  
 410 at each wavelength and 17 isotopologues) provide the necessary data required by the LAD  
 411 method to systematically dismiss outlier data points produced by noisy conditions. The  
 412 implementation of the LAD method reduces the random character of noise in the measured  
 413 intensities to partially convert it into a systematic error. Calculated  ${}^{3x}J$  values were compared  
 414 to calculations under the same solar spectra for cross-sections reported by Danielache et al.  
 415 (2008, 2012) measured at  $25 \text{ cm}^{-1}$  and  $8 \text{ cm}^{-1}$  numbers respectively. **Figure 10** compares these  
 416 three data sets. One clear and counter intuitive trend is that the higher the spectral resolution  
 417 the smaller the differences among  ${}^{3x}J$  values. This trend has also been observed by Endo et al.  
 418 (2015) for the  $\tilde{C} - \tilde{X}$  absorption band. The comparison is a clear reminder that when  
 419 considering light induced isotopic effects predictions from single or a narrow band of  
 420 wavelengths. Error bars for values measured at  $8 \text{ cm}^{-1}$  spectral resolution for  ${}^{33}J$  and  ${}^{34}J$  clearly  
 421 overlap casting shadows on the reliability of the derived isotopic enrichment factors. The  $J$   
 422 values presented in this report present error bars which are far smaller than the  $J$  values  
 423 themselves. Calculated  ${}^{3x}\varepsilon$  and  ${}^{3x}E$  are, as expected, similar in both methods while  $\sigma^{3x}\varepsilon$  and  
 424  $\sigma^{3x}E$  values obtained from the cross-sections calculated with the LAD are 1 order of magnitude  
 425 smaller than those obtained by the averaging method (**Tables 3 and 4**).

426 **Table 2.** Calculated photoexcitation rate constants ( ${}^{3x}J$ ) and propagated standard deviations  
 427 ( $\sigma^{3x}J$ ). All values are in molecules  $\text{cm}^{-3} \text{ s}^{-1}$  units.

	${}^{32}J$	${}^{33}J$	${}^{34}J$	${}^{36}J$	$\sigma^{32}J$	$\sigma^{33}J$	$\sigma^{34}J$	$\sigma^{36}J$
LAD Method	$3.0913 \times 10^{-3}$	$3.0982 \times 10^{-3}$	$3.1097 \times 10^{-3}$	$3.1137 \times 10^{-3}$	$7.03 \times 10^{-7}$	$4.41 \times 10^{-7}$	$4.42 \times 10^{-7}$	$3.96 \times 10^{-7}$
Averaging Method	$3.090 \times 10^{-3}$	$3.097 \times 10^{-3}$	$3.108 \times 10^{-3}$	$3.113 \times 10^{-3}$	$1.42 \times 10^{-5}$	$1.42 \times 10^{-5}$	$1.44 \times 10^{-5}$	$1.44 \times 10^{-5}$

428

429

430 **Table 3.** Calculated isotopic enrichment factors ( $^{3x}\epsilon$ ) during photoexcitation and propagated  
 431 standard deviations ( $\sigma^{3x}\epsilon$ ). All values are in permil (‰) units.

	$^{33}\epsilon$	$^{34}\epsilon$	$^{36}\epsilon$	$\sigma^{33}\epsilon$	$\sigma^{34}\epsilon$	$\sigma^{36}\epsilon$
LAD Method	5.91	2.22	7.22	0.26	0.26	0.26
Averaging Method	5.84	2.13	7.29	6.51	6.49	6.52

432

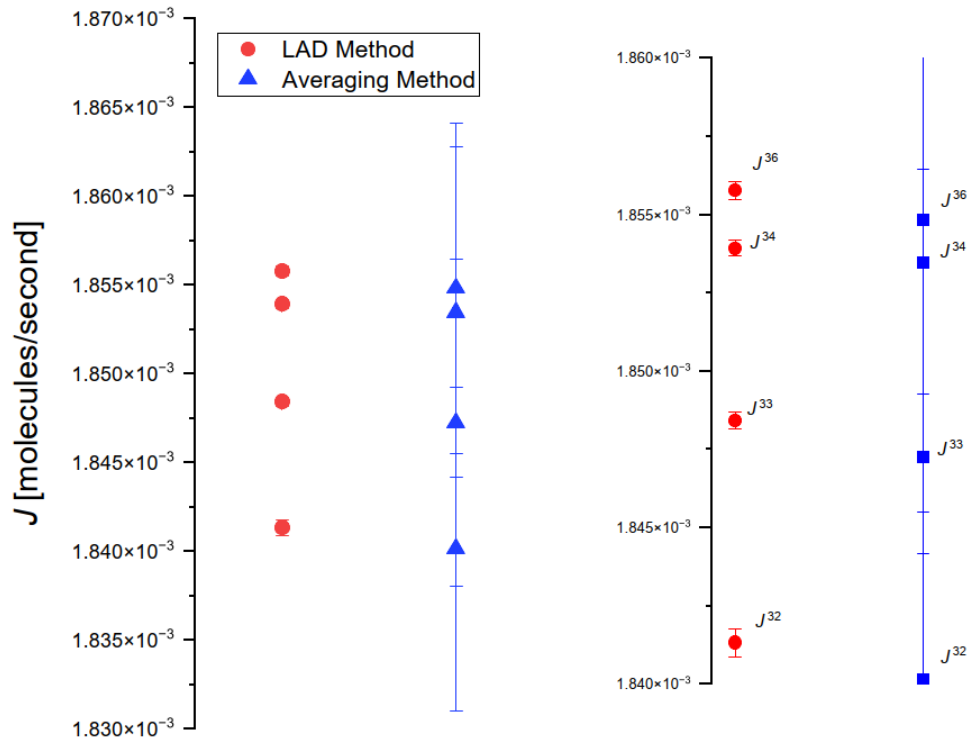
433 **Table 4.** Calculated mass independent isotopic enrichment factors ( $^{3x}E$ ) during photoexcitation  
 434 and propagated standard deviations ( $\sigma^{3x}E$ ). All values are in permil (‰) units.

	$^{33}E$	$^{36}E$	$\sigma^{33}E$	$\sigma^{36}E$
LAD Method	-0.83	-4.02	0.19	0.36
Averaging Method	-0.88	-3.81	5.64	10.76

435

436 The introduction of the LAD method has made possible the reduction of propagated error bars  
 437 to a point where reliable geochemical predictions are possible. Spectral resolution has also been  
 438 a topic of concern. Previous measurements by Danielache et al. (2008, 2012) carried out at a  
 439 spectral resolution of 25 cm<sup>-1</sup> and 8 cm<sup>-1</sup> respectively, the relation between spectral resolution  
 440 and predicted isotopic effect has been so far acknowledged but not properly addressed. A  
 441 definite study on the quantitative relation between isotopic effect and spectral resolution is yet  
 442 to be done. Rufus et al. (2003) reported absorption cross for this band at a spectral resolution  
 443 between 0.04 cm<sup>-1</sup> and 0.13 cm<sup>-1</sup>, which is according with their assessment sufficient to resolve  
 444 all natural line widths. For the measurements in this report the optimal trade-off between  
 445 spectral resolution and spectral noise was set to 0.4 cm<sup>-1</sup>. Based on recent reports on pressure  
 446 broadening (Lyons et al., 2018) and line profile density (Kumar et al., 2015) suggest that a  
 447 spectral resolution 0.4 cm<sup>-1</sup> could be sufficient for the study of photochemical induced isotopic  
 448 effects at about 1 atm of pressure.

449 The calculated  $^{34,33,36}\epsilon$  and  $^{33,36}E$  (**Figure 11**) enrichment factors derived from this and previous  
 450 measurements are compared respect to spectral resolution at each measurement. All  $^{3x}J$  values  
 451 were calculated for a top of the atmosphere with a solar flux reported by Gueymard (2004) and  
 452 adjusted to the spectral resolution of this report. Danielache et al. (2008) first presented  
 453 spectrum of  $^{32,33,34}\text{SO}_2$  but used natural abundance  $\text{SO}_2$  as  $^{32}\text{S}$  18 isotopologues, and a spectral  
 454 resolution ~25 cm<sup>-1</sup>. These first measurements were conducted at the very early stages of this  
 455 decade long enquiry, they were designed for the  $\tilde{C} - \tilde{X}$  absorption band and issues of spectral  
 456 resolution were not properly taken into account. Danielache et al. (2012) later improved the  
 457 sample preparation and conducted the measurements at a higher resolution data (~8 cm<sup>-1</sup>), and  
 458 higher S/N ratios achieving propagated small error bars. This study introduced a new algorithm  
 459 to further reduce the errors associated with increased resolution and the number of  
 460 measurements at each pressure were extended the statistical maximum. The comparison in  
 461 **Figure 11** suggest, yet do not quantitatively prove, that the higher the spectral resolution, the  
 462 smaller the isotopic effect for all  $^{34,33,36}\epsilon$  and  $^{33,36}E$  values.

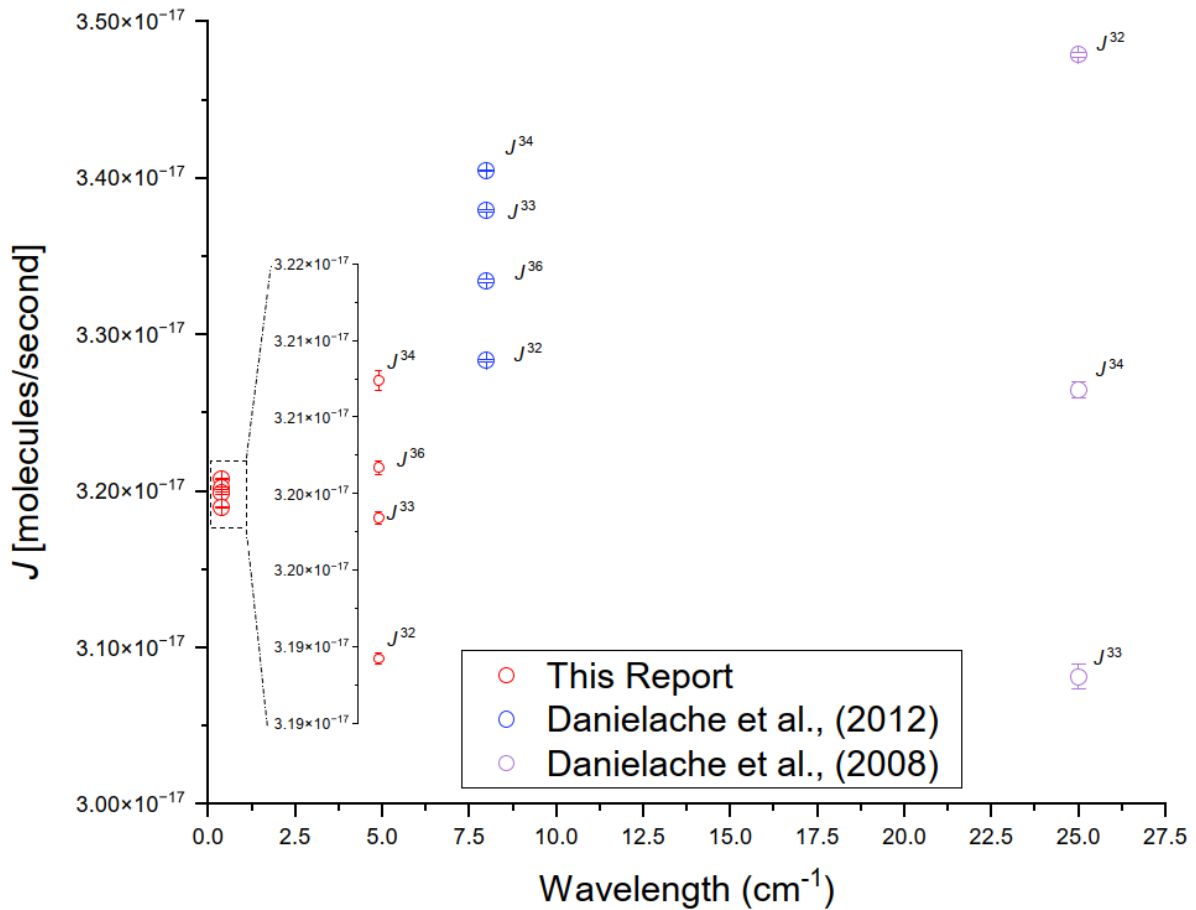


463

464 **Figure 9:** Photoexcitation rate constants calculated for a present Earth top of the atmosphere  
 465 (TOA) conditions with actinic flux reported by (Gueymard, 2004)) for measured  $^{32}\text{SO}_2$ ,  $^{33}\text{SO}_2$ ,  
 466  $^{34}\text{SO}_2$ , and  $^{36}\text{SO}_2$  isotopologues. The red and blue data sets represent cross-sections derived the  
 467 LAD and averaging methods respectively. Both methods yield nearly the same  $J$  values.  
 468 Propagated errors by the averaging method (red) produce error bars that overlap  $J$  values  
 469 rendering them unreliable to geochemical predictions. The implemented LAD method (blue  
 470 data sets) solves this problem.

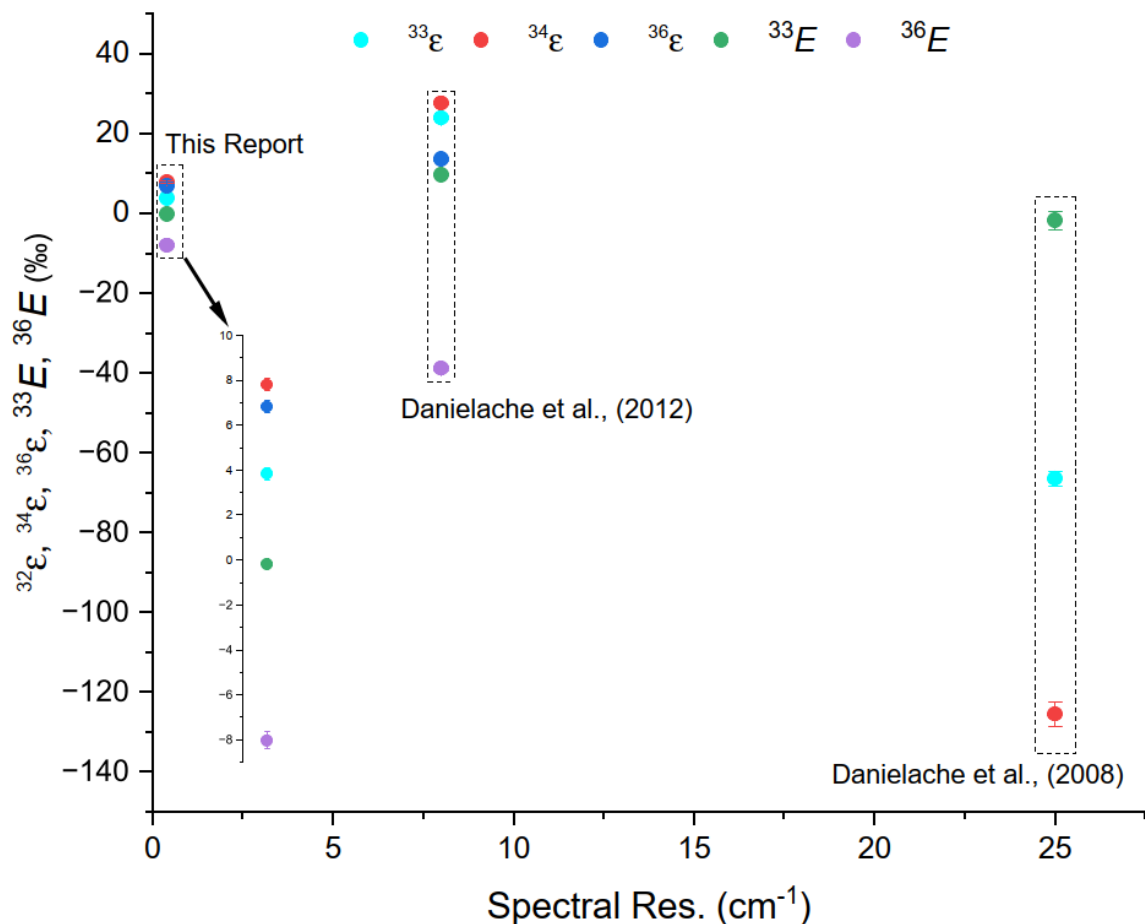
471

472



473

474 **Figure 10:** Photoexcitation rate constants calculated for a present Earth top of the atmosphere  
 475 (TOA) conditions with actinic flux reported by (Gueymard, 2004)) for measured <sup>32,33,34</sup>SO<sub>2</sub>  
 476 isotopologues and compared to previously reported by Danielache et al. (2008, 2012). The  
 477 newly reported data sets (black) have propagated error bars that are smaller than the differences  
 478 between calculated *J* values therefore making them reliable for geochemical predictions.



479

480 **Figure 11:** Relationship between isotopic fractionation  $^{34,33,36}\epsilon$  and  $^{33,36}E$  vs. spectral resolution  
 481 calculated from data in this report and compared to previously reported data by Danielache at  
 482 al. (2008, 2012). The comparison of the data sets shows a clear trend where isotopic effects  
 483 tend to be smaller with increased spectral resolution.

484

### 485 3.2 Comparison with isotope fractionation observed in SO<sub>2</sub> photochemical experiments

486 Sulfur isotope fractionation during SO<sub>2</sub> photoexcitation at wavelengths in the  $\tilde{B} - \tilde{X}$  band  
 487 was investigated by UV irradiating SO<sub>2</sub> with natural isotope ratios and examining the sulfur  
 488 isotope ratios of the products (referred to as SO<sub>2</sub> photochemical experiments below) (Endo et  
 489 al., 2016; Whitehill and Ono, 2012; Whitehill et al., 2013)). Quadruple sulfur isotope analysis  
 490 of the products show large S-MIF, with  $\Delta^{33}\text{S}$  up to 78‰ (Whitehill et al., 2013) and up to 142‰  
 491 (Endo et al., 2016) with positive  $\Delta^{36}\text{S}/\Delta^{33}\text{S}$  ratios. In this section, we compare isotope  
 492 fractionation factors predicted from our absorption cross-section measurements with those  
 493 previously observed in SO<sub>2</sub> photochemical experiments. Then, we discuss the origin of S-MIF,  
 494 which occurs in SO<sub>2</sub> photoexcitation or related to the reaction.

495 Whitehill et al. (2013)) irradiated SO<sub>2</sub> with UV light under N<sub>2</sub> bath gas and measured quadruple  
 496 sulfur isotopes of produced organics. They used a Xe arc lamp as a broadband UV source and  
 497 controlled UV spectra with UV filters to prevent SO<sub>2</sub> photolysis and examine the wavelength  
 498 dependence of the isotope fractionations. Acetylene was added as an electron donor in the

499 experiments. Although reactions are not fully understood, some organic sulfur matter was  
 500 produced and collected after UV irradiation. The expected relevant chemical pathways during  
 501 this experiment are reactions 1 to 4 (R1-R4) (e.g., Heicklen et al., 1980)



506 The notation used in reactions 1 to 4 (R1 to R4) describe specific electronic and vibrational  
 507 states and are not frequent in chemical notation. Starting with R1  $\text{SO}_2(^1\text{A}_1)$  is the electronic  
 508 ground state with a given and unspecified rovibrational state.  $\text{SO}_2(^1\text{A}_2 \nu=n)$  and  $\text{SO}_2(^1\text{B}_1 \nu=n)$   
 509 are the photoexcited electronic  $^1\text{A}_2/^1\text{B}_1$  manifold (mixing of two electronic states) at a given  $n$   
 510 vibrational state (this fragment is also commonly known as  $\text{SO}_2^*$ ). In R2 M is a third body  
 511 collider (e.g.,  $\text{N}_2$ ) which triggers a quenching reaction to produce the electronic  $^1\text{A}_2$  state at its  
 512 ground rovibrational state ( $\nu=0$ ). R3 shows the intersystem crossing (ISC) from the singlet  $^1\text{A}_2$   
 513 ( $\nu=0$ ) state to the triplet ( $^3\text{B}_1$ ). Because  $\text{SO}_2(^3\text{B}_1)$  is more reactive than  $\text{SO}_2(^1\text{A}_2/^1\text{B}_1)$  (Kroll et  
 514 al., 2018)  $\text{SO}_2(^3\text{B}_1)$  reacts (R3) selectively with acetylene. The details of the reaction R4 have  
 515 yet to be understood, but they are unlikely to significantly contribute to S-MIF.

516 Isotopic fractionation factor in reaction R1 is predicted with absorption cross-sections of  $\text{SO}_2$   
 517 isotopologues measured by this study and Danielache et al. (2012). Reactions other than  
 518 reaction R1 also may contribute to the isotopic fractionation observed in photochemical  
 519 experiments. Whitehill et al. (2013) suggested that reaction R2 mainly originated the observed  
 520 S-MIF in their experiments, mainly because (1) their theoretical study suggests that isotope  
 521 selective intersystem crossing might potentially contribute to the observed S-MIF and (2) their  
 522 results significantly differ from the S-MIF in reaction R1 predicted with  $\text{SO}_2$  absorption cross-  
 523 sections measured by Danielache et al. (2012) (Fig. 13).

524 Furthermore, the observed MIF signature is considerably different from those predicted by  
 525 isotopologue-specific absorption cross-sections. They also show that excitation wavelength  
 526 range produces isotopic effects in the order of 20-60‰ for  $\Delta^{36}\text{S}$  and 10-40‰ for  $\Delta^{33}\text{S}$ . The  
 527 wavelength range-isotopic effect is significant yet not as large as the pressure dependency  
 528 observed when the full spectral region of the  $\tilde{\text{A}}^1\text{A}_2/\tilde{\text{B}}^1\text{B}_1$  manifold was photoexcited  
 529 (Whitehill et al., 2013, Fig. 2).

530 To compare our results with those of Whitehill et al. (2013), we calculate fractionation factors  
 531 using  $\text{SO}_2$  absorption cross-sections of this study and Danielache et al. (2012) from Eqs. (11)  
 532 to (14), assuming a 150 W Xenon arc lamp spectrum and absorption spectra with UV filters.  
 533 The comparisons are shown in **Figures 12** and **13** where the isotopic effect produced during  
 534 the photoexcitation process (R1) is compared to the results from chamber experiments.

535 **Figure 12** compares  $\Delta^{33}\text{S}$ ,  $^{33}\text{E}$  values to  $\delta^{34}\text{S}$ ,  $^{34}\text{E}$ . The values reported by Whitehill et al. (2013),  
 536 regardless of excitation wavelength region or  $P_{\text{SO}_2}$  do not match the ones calculated from the

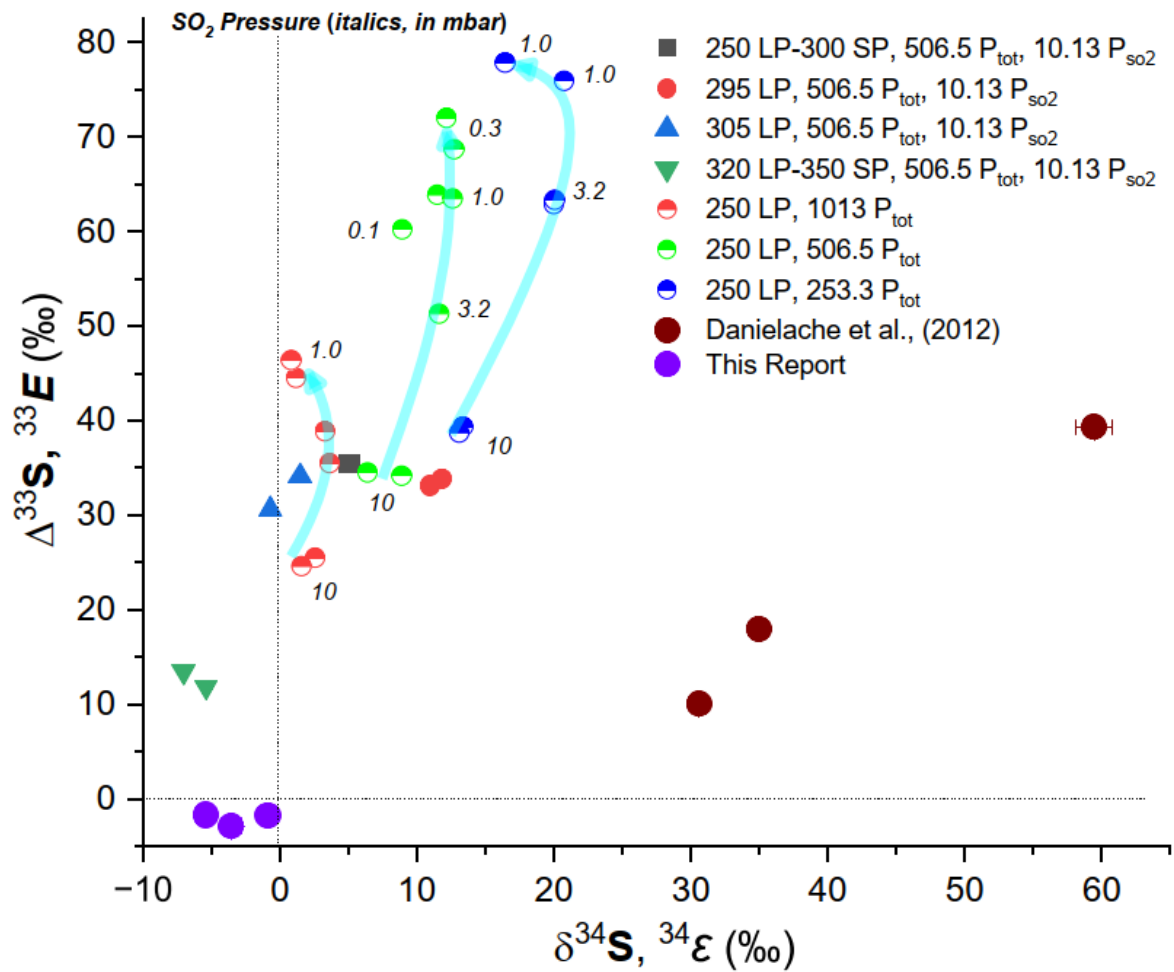
537 spectra reported by Danielache et al. (2008) neither the ones calculated from the spectra in this  
538 report. Large discrepancies are also observed on **Figure 13** where small and negative values of  
539  $^{33}E$  and  $^{36}E$  from spectra in this report show no correlation with large and positive  $\Delta^{36}S$  and  
540  $\Delta^{33}S$  isotopic ratios from the chamber experiments. Self-shielding calculations reported by  
541 Whitehill et al. (2013) and photoexcitation induced enrichment factors calculated from data  
542 reported by Danielache et al. (2008) and photoexcitation effects from the same spectra at  
543 different spectral ranges independently calculated in this report, show large negative  $^{36}E$  and  
544 large positive  $^{33}E$  values which don't match chamber experiments either.

545

546 From the comparisons in **Figures 12** and **13** the data presented in this report tend to support  
547 the conclusions reported by Whitehill et al. (2013) that the MIF isotopic ratios measured in  
548 collected organosulfur are likely produced by the ISC process in R3. Furthermore, the data in  
549 this report in which values of  $^{34}\epsilon$ ,  $^{33}E$  and  $^{36}E$  being small and quite insensitive to the excitation  
550 wavelength band could contribute to the final organosulfur product MIF. This hypothesis does  
551 not provide any explanation to the large  $\Delta^{33}S$ ,  $\Delta^{36}S$  values to  $\delta^{34}S$  values reported from chamber  
552 experiments under different band-pass filters, partial  $SO_2$  and total  $N_2$  pressures.

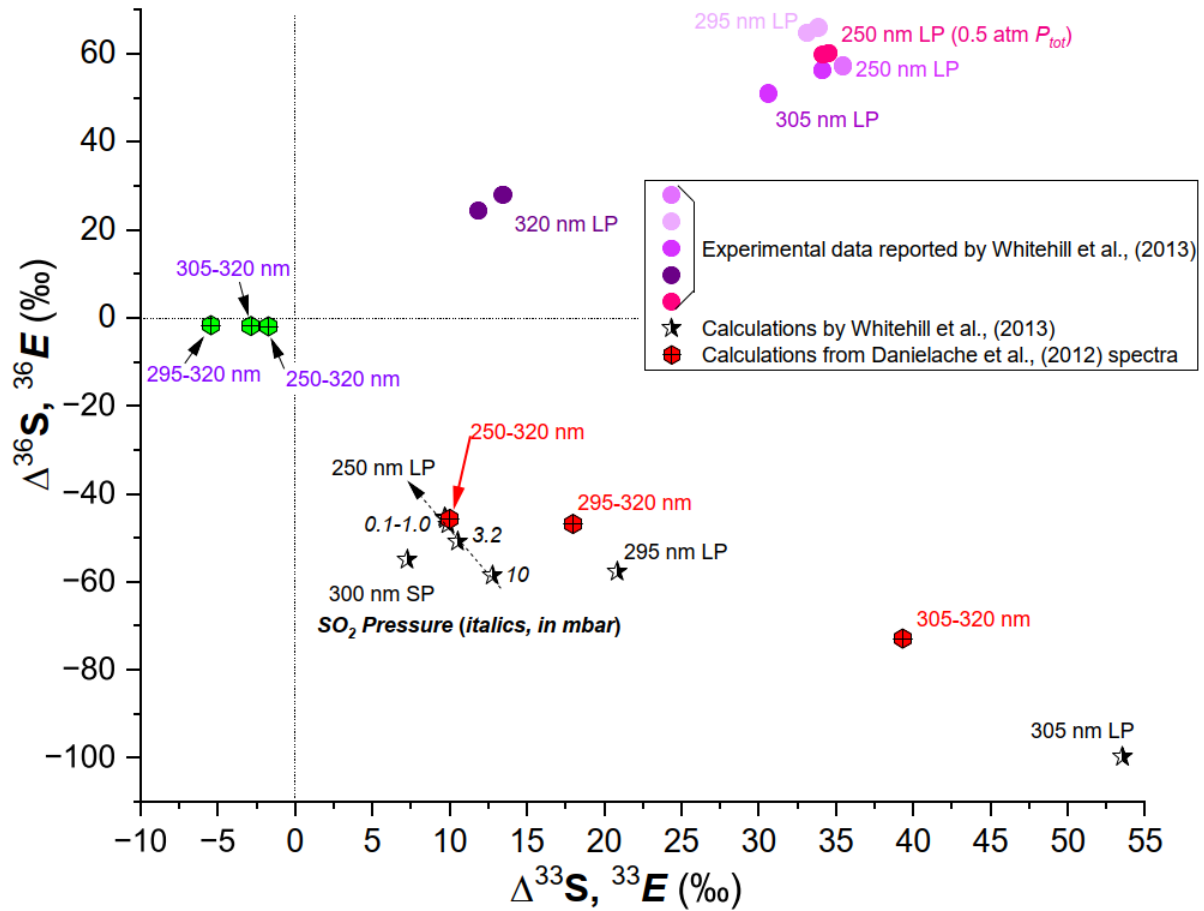
553

554



555

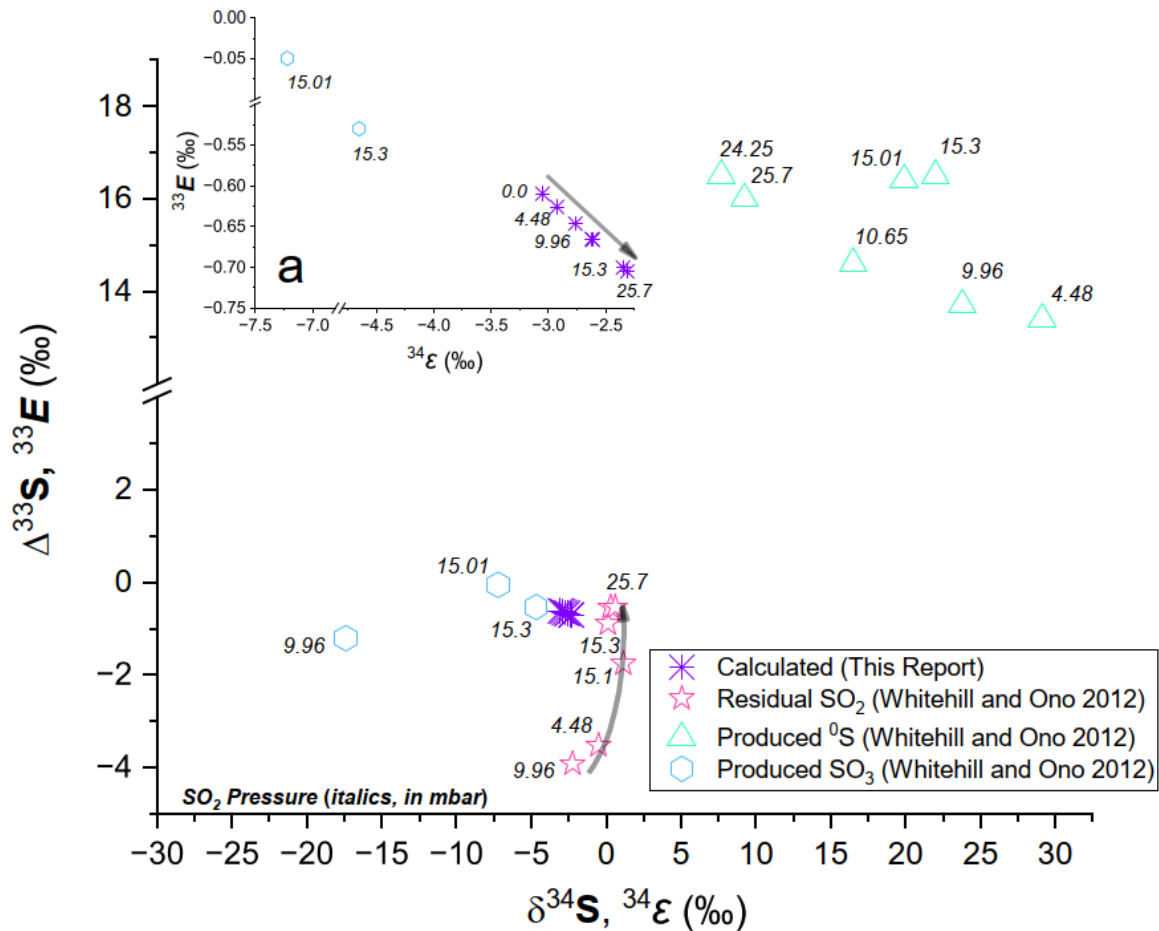
556 **Figure 12:** Calculated  $^{34}\epsilon$  vs.  $^{33}E$  isotopic effects from spectra reported by Danielache et al.  
 557 (2012) and from spectra reported in this study using a 150W Xenon arc lamp spectrum and  
 558 compared to experiments by Whitehill et al. (2013)) ( $\delta^{34}S$  and  $\Delta^{33}S$ ). The units of the spectral  
 559 range are in nm, while P<sub>tot</sub> (total gas pressures) and P<sub>SO<sub>2</sub></sub> (partial pressures of SO<sub>2</sub>) are in mbar.  
 560



561

562 **Figure 13:** Calculated  $^{33}E$  vs.  $^{36}E$  isotopic effects from spectra reported by Danielache et al.  
 563 (2012) and from spectra reported in this study using a 150W Xenon arc lamp spectrum and  
 564 compared to experiments by Whitehill et al. (2013) ( $\Delta^{33}S$  and  $\Delta^{36}S$ ).  $P_{tot}$  (total gas pressures)  
 565 and  $P_{SO_2}$  (partial pressures of  $SO_2$ ) are expressed in mbar units.  
 566

567 In order to assess the difference between the isotopic imprint between R1 and R3, next  
 568 photoexcitation rate constants from isotopic-specific spectra in the 250–320 nm region were  
 569 calculated and compared to chamber experiments reported by Whitehill and Ono (2012).  
 570  
 571



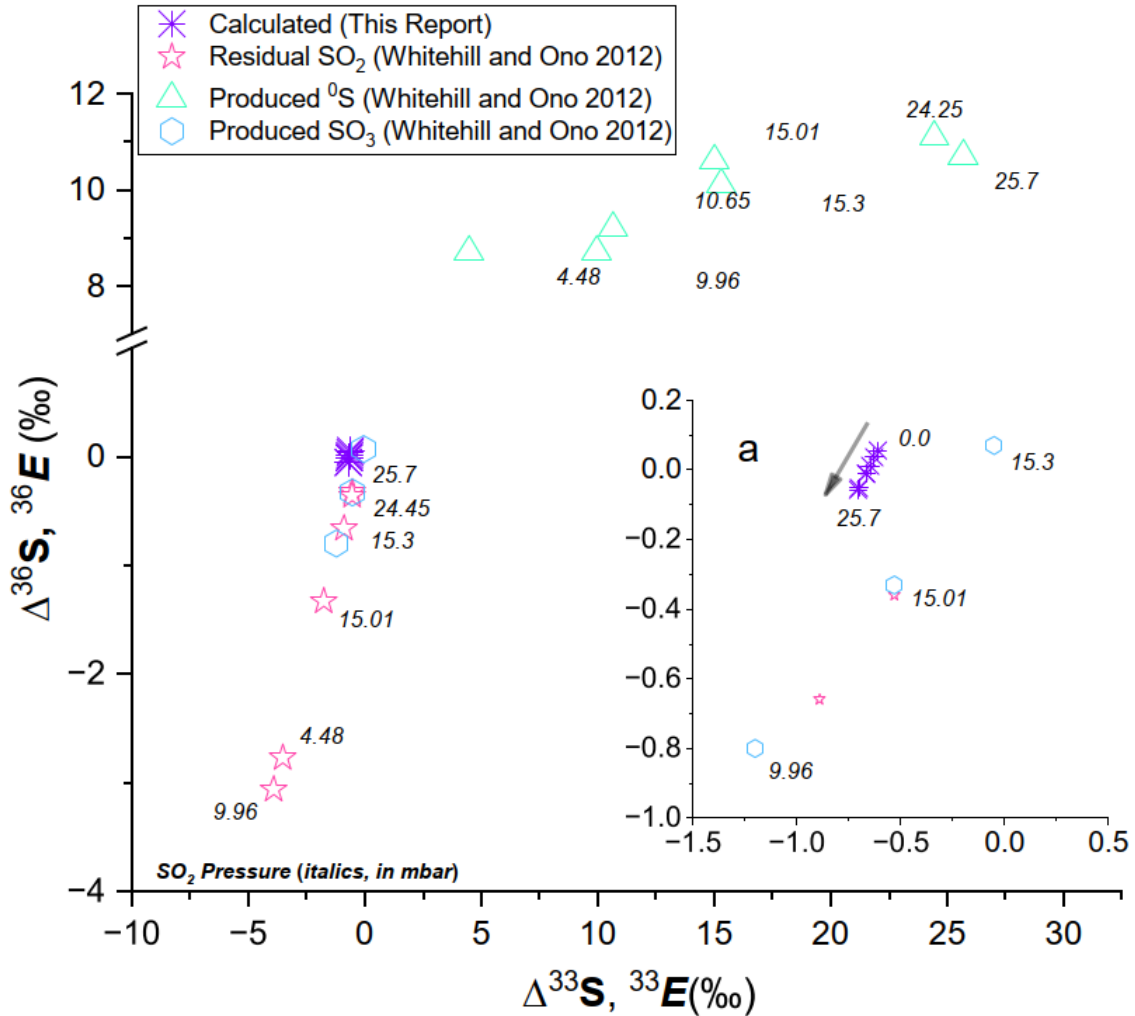
572

573 **Figure 14:** Calculated  $^{34}\epsilon$  vs.  $^{33}E$  isotopic effects from spectra reported in this study using a  
 574 150W Xenon arc lamp spectrum and compared to experiments by Whitehill et al., 2013) ( $\delta^{34}S$   
 575 and  $\Delta^{33}S$ ).

576

577 Experiments conducted by Whitehill and Ono (2012) where they focused on isotopic mixing  
 578 ratios ( $\delta^{34}S$  vs.  $\Delta^{33}S$  and  $\Delta^{33}S$  vs.  $\Delta^{36}S$ ) of oxydation products of photoexcited ( $^1B_1$   $^1A_2$ )SO<sub>2</sub>  
 579 and residual ground state SO<sub>2</sub>. For additional insight a simple self-shielded photoexcited  
 580 enrichment factors ( $^{34}\epsilon$  vs.  $^{33}E$  and  $^{33}E$  vs.  $^{36}E$ ) at pressures ranging from 4.48 to 25.7 mbar  
 581 using a 150W Xenon arc lamp spectrum was added to the analysis. The results are presented  
 582 in **Figures 14** and **15**. **Figure 14** shows that calculated enrichment factors  $^{34}\epsilon$  and  $^{33}E$  present  
 583 clearly different values to isotopic mixing ratios  $\delta^{34}S$  vs.  $\Delta^{33}S$  for produced  $^0S$  (Whitehill and  
 584 Ono, 2012). Residual SO<sub>2</sub> show negative values of  $\delta^{34}S$  and  $\Delta^{33}S$ , for experiments conducted  
 585 at 25.7 mbar of partial pressure of SO<sub>2</sub>, are quite similar to those calculated in this report. Most  
 586 significantly, the calculated  $^{34}\epsilon$  and  $^{33}E$  values are not only very close to those reported by  
 587 Whitehill and Ono (2012) for produced SO<sub>3</sub>, but they also have a very similar slope (inset **a**).  
 588 The comparisons in **Figure 15** are even more revealing since  $^{33}E$  vs.  $^{36}E$  slope calculated from  
 589 spectra in this report almost perfectly match the  $^{33}E$  vs.  $^{36}E$  slope reported by Whitehill and  
 590 Ono (2012) for produced SO<sub>3</sub>, and residual SO<sub>2</sub>. Furthermore, in both cases the  $^{36}E/^{33}E$  and  
 591  $\Delta^{36}S/\Delta^{33}S$  slopes are particularly identical (**Figure 15** inset **a** for clarity). From the above  
 592 discussion it can be suggested that the ( $^1B_1$   $^1A_2$ )SO<sub>2</sub> photoexcitation band is likely to have a

593 small isotopic effect that is transported to the SO<sub>3</sub> products. A quantitative mass balance  
 594 analysis of the reaction products and residuals is necessary for obtaining further insight into  
 595 the processes taking place at the chamber experiments reported by Whitehill and Ono (2012)  
 596 and Whitehill et al. (2013).  
 597  
 598



599  
 600 **Figure 15:** Calculated  $^{33}\text{E}$  vs.  $^{36}\text{E}$  isotopic effects from spectra reported in this study using a  
 601 150W Xenon arc lamp spectrum and compared to experiments by Whitehill et al. (2013)) ( $\Delta^{33}\text{S}$   
 602 and  $\Delta^{36}\text{S}$ ).  
 603

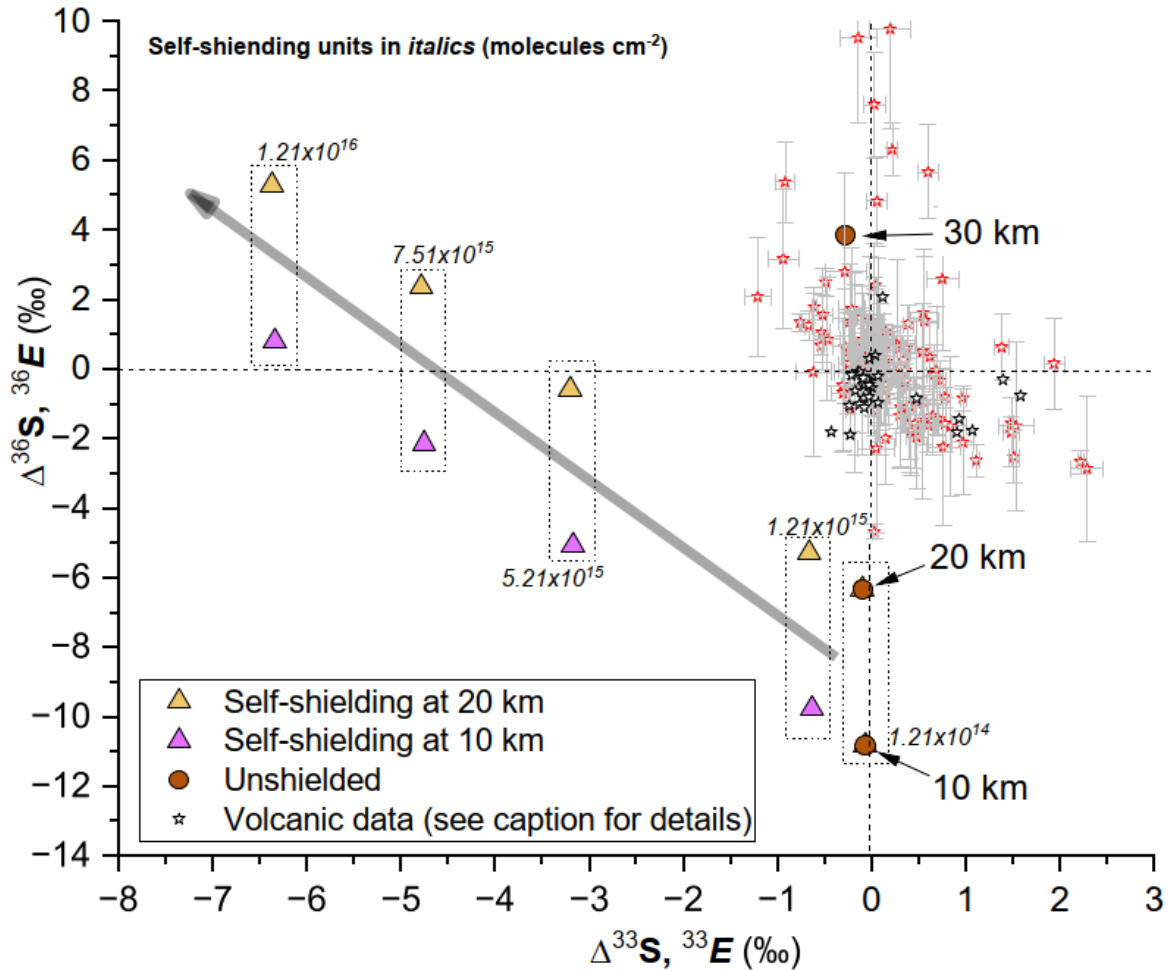
604 **3.4 Geochemical implications**

605 The origin of S-MIF found in stratospheric sulfate aerosols (SSA) is still debated. Savarino et  
 606 al. (2003) attributed the S-MIF to SO<sub>2</sub> photoexcitation, because the SSA array of  $\Delta^{36}\text{S}/\Delta^{33}\text{S} \approx$   
 607  $-4.3$  matched early photoexcitation experimental results where KrF excimer laser (248 nm of  
 608 narrow band) was used ( $\Delta^{36}\text{S}$  vs  $\Delta^{33}\text{S}$  slope  $\approx -4.2$ ; Farquhar et al., 2001). It is suspected that  
 609 experiments using narrow-band UV spectra, which are significantly different from the sunlight  
 610 spectrum, do not simulate isotope fractionation in the atmosphere (e.g., Claire et al., 2014).  
 611 Subsequently, Danielache et al. (2012) reported  $^{32,33,34,36}\text{SO}_2$  absorption cross-section

612 measurements for the  $\tilde{B}^1B_1-\tilde{X}^1A_1$  band, allowing predictions of sulfur isotopic compositions  
 613 in sulfate aerosols under various atmospheric conditions. Then, Hattori et al. (2013) modeled  
 614 chemical reaction networks with a one-box model and calculated the isotope ratio of sulfate,  
 615 assuming that SO<sub>2</sub> photoexcitation causes MIF with the <sup>32,33,34,36</sup>SO<sub>2</sub> absorption cross-section  
 616 measurements. The results of  $\Delta^{33}\text{S}$  magnitudes and  $\Delta^{36}\text{S}/\Delta^{33}\text{S}$  ratios in sulfates reproduce those  
 617 within the SSA array. Thus, it is suggested that SO<sub>2</sub> photoexcitation (reaction R1) is the origin  
 618 of the S-MIF in SSA. However, this result strongly depends on the results of the absorption  
 619 cross-section measurements by Danielache et al. (2012). In this section we compare  
 620 photoexcitation induced enrichment factors calculated from reported cross-sections to ice core  
 621 data reported by Gautier et al. (2018), Shaheen et al. (2013) and Baroni et al. (2008). Gautier  
 622 et al. (2018) have updated  $\Delta^{36}\text{S}/\Delta^{33}\text{S}$  ratio to  $-1.56 \pm 0.25$  for records of the past 2,600 years,  
 623 further modeling is required to explain the discrepancies between models based on spectra and  
 624 observations. However, the  $\Delta^{36}\text{S}/\Delta^{33}\text{S}$ 's difference of the updated data by Gautier et al. (2018)  
 625 may not be significant to determine the origin of S-MIF. The  $\Delta^{36}\text{S}/\Delta^{33}\text{S}$  slope can be changed  
 626 by mixing processes between mass-independent and mass-dependent sulfur species, that is,  
 627 when non-zero  $\Delta^{33}\text{S}$  signature is “diluted.” This process happens because of the non-linearity  
 628 character of the  $\Delta^{33}\text{S}$  and  $\Delta^{36}\text{S}$  definitions (Endo et al. under review).  
 629 Attenuation by atmospheric shielding of UV light below 300 nm renders all possible  
 630 photoexcitations unlikely below 10 km. At an altitude of 30 km, the band of available UV  
 631 radiation expands to 290 nm, and at an altitude of 40 km, UV light with wavelength longer  
 632 than 280 nm can participate in the reaction. At 50 km of altitude, the atmospheric shielding  
 633 effect significantly weakens, and the entire SO<sub>2</sub> UV absorption  $\tilde{B}^1B_1-\tilde{X}^1A_1$  band contributes  
 634 to the photoexcitation process (See **Figure S7**). Solar flux at different altitudes generates  
 635 different S-MIF signatures on the SO<sub>2</sub> photoexcitation reaction. Solar flux at different altitudes  
 636 used in the calculation of altitude dependent photoexcitation rate constants were obtained from  
 637 modelled current atmosphere (Danielache et al., 2023) using actinic solar flux (Gueymard,  
 638 2004) at the top of atmosphere. The results of isotopic fractionation of self-shielding free SO<sub>2</sub>  
 639 photoexcitation reaction (250–320 nm) are shown in **Figure 16** (brown circles).  
 640 The same calculation at different altitudes combined with self-shielding under an SO<sub>2</sub> column  
 641 density ranging from  $1.21 \times 10^{14}$  to  $1.21 \times 10^{16}$  molecules cm<sup>-2</sup> are shown in **Figure 16** (violet  
 642 and yellow triangles), and for SO<sub>2</sub> column densities up to  $1.21 \times 10^{17}$  molecules cm<sup>-2</sup> which are  
 643 closer to those reported during the Pinatubo eruption are presented in **Figure 17**. For a further  
 644 comparison, comparisons isotopic effects calculated by Hattori et al. (2013) are added to **Figure**  
 645 **17**. **Figure 16** also shows volcanic data from Gautier et al. (2018) (red stars), Shaheen et al.,  
 646 (2014) (black stars) and Baroni et al., (2008) (violet stars). Self-shielding free photoexcitation  
 647 effect is almost 0 in <sup>33</sup>E and stays unchanged with altitude, <sup>36</sup>E range from -10‰ at 10 km to  
 648 4‰ at 30 km. Altitude variability do not produce any significant <sup>36</sup>E/<sup>33</sup>E slope but it they show  
 649 an interesting overlap with volcanic data suggesting that the <sup>36</sup>E variability is produced by  
 650 altitude. Self-shielding calculations show a more revealing result in which increased column  
 651 density (up to  $1.21 \times 10^{16}$  molecules cm<sup>-2</sup>) creates a <sup>36</sup>E/<sup>33</sup>E slope compatible with the reported  
 652 volcanic data. The data presented in **Figure 17** includes the data in **Figure 16** but it has  
 653 expanded both <sup>33</sup>E and <sup>36</sup>E axis. By expanding the <sup>33</sup>E and <sup>36</sup>E axis, self-shielding calculations  
 654 more realistic to a stratospheric eruption ( $1.21 \times 10^{17}$  molecules cm<sup>-2</sup>) shows that the slope does  
 655 not change but also is compatible and of reverse signs to the altitude and self-shielding

656 calculations of Hattori et al. (2013) and also  $^{36}E/^{33}E$  slope compatible with volcanic reported  
 657 data.

658

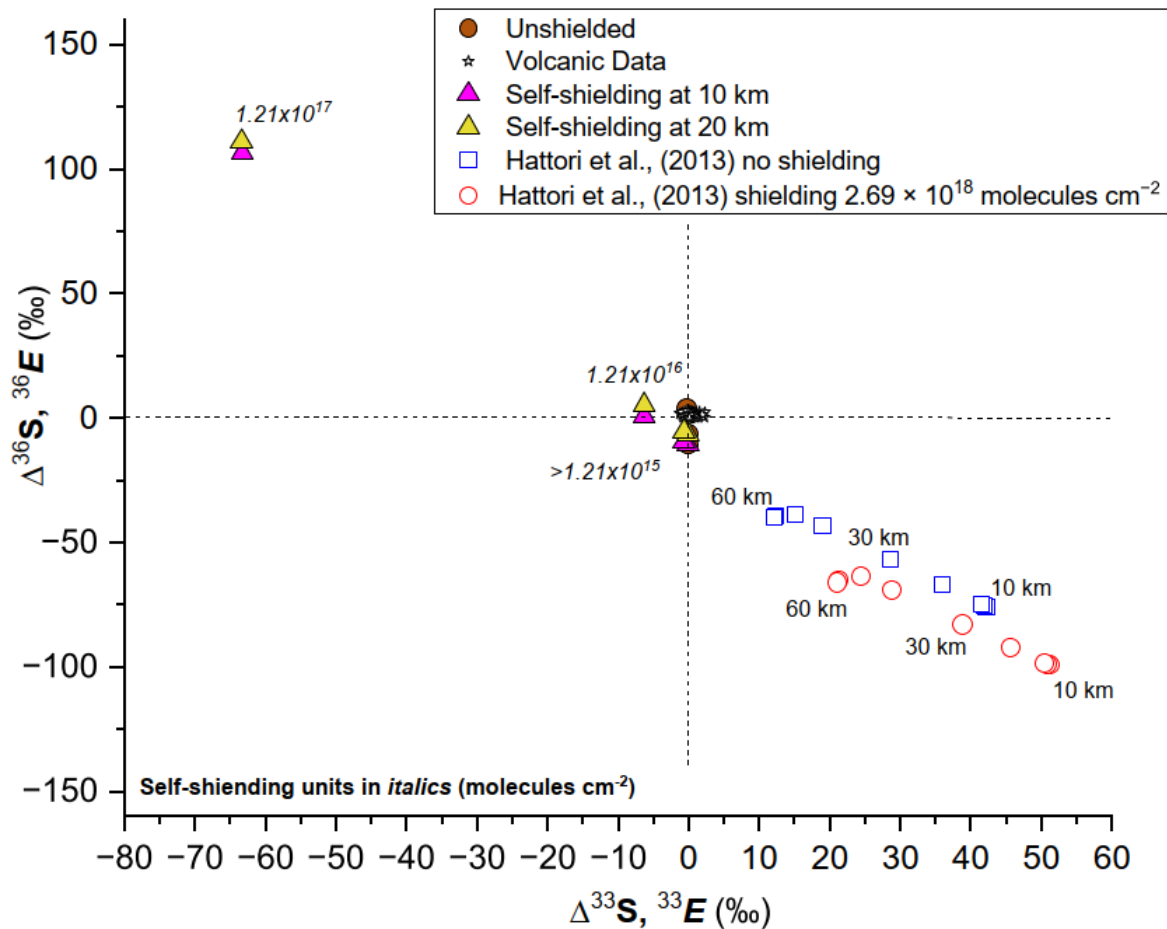


659

660 **Figure 16:** The isotopic fractionation from SO<sub>2</sub> photoexcitation using modern atmospheric  
 661 solar flux at different altitudes and comparison with Hattori et al. (2013). (a)  $^{34}E$  and  $^{33}E$ . (b)  
 662  $^{33}E$  and  $^{36}E$ . The volcanic data is from Gautier et al. (2018) (red stars), Shaheen et al. (2013)  
 663 (black stars) and Baroni et al. (2008) (violet stars).

664

665



666

667 **Figure 17:** Photoexcitation enrichment factors calculated from this report compared to those  
 668 reported by Hattori et al. (2013). Self-shielding calculation with column densities of  $10^{19}$   
 669 molecules  $\text{cm}^{-2}$  (530 DU) as suggested by Guo et al. (2004) produced values of  $^{36}E = 1.314\text{‰}$   
 670 and  $^{33}E = 1.163\text{‰}$  which fall well outside of the range in the plot.

671

## 672 4 Conclusions

673 This study presents the cross-sections of  $^{32}\text{SO}_2$ ,  $^{33}\text{SO}_2$ ,  $^{34}\text{SO}_2$ , and  $^{36}\text{SO}_2$  for the  $\tilde{B}^1B_1-\tilde{X}^1A_1$   
 674 absorption band at 293.15 K measured at a resolution of  $0.4\text{ cm}^{-1}$  with an error of 3–10%. In  
 675 this report we implemented an algorithm using the LAD linear regression which was applied  
 676 to finely calibrate the linear relationship between absorbance and pressure and then achieve the  
 677 cross-section data at each wavelength. The overall features of measured cross-sections, that is,  
 678 the peak positions of isotopologues, are consistent with previous studies (Danielache et al.,  
 679 2008; Danielache et al., 2012). We obtained both more detail in the absorption peaks and a  
 680 significant improvement in errors derived from noise during the measurement. For S-MIF  
 681 related to  $\text{SO}_2$  photochemistry, S-MIF predicted from our new spectral measurements do not  
 682 reproduce results of S-MIF observed in  $\text{SO}_2$  photochemical experiments performed by  
 683 Whitehill et al. (2013). The discrepancy supports Whitehill's argument that large S-MIF  
 684 originates in the intersystem crossing rather than photoexcitation alone.

685

**686 Acknowledgements**

687 This study does not have real or perceived financial conflict of interest for any author. We  
688 would like to thank Shohei Hattori and Naohiro Yoshida for sample preparation and Matthew  
689 S. Johnson for technical advice. We also wish to thank Yi Ding for his consultation and advice  
690 on machine learning and algorithms. This research was funded by JSPS KAKENHI (grant  
691 numbers 22H05150 and 20H01975).

**692 Data Availability Statement**

693 The spectral data presented in this manuscript was recorded at the Tokyo Institute of  
694 Technologies with experimental devices described in the experimental section. Reported data  
695 set in this study are available at Harvard Dataverse repository of research data via  
696 <https://doi.org/10.7910/DVN/AP8ISE> with CC0 1.0 license/Data use agreement. Figures were  
697 made with Origin Ver. 2022 (Origin Lab). The code used in this manuscript for the calculation  
698 of absorption cross-sections is licensed under MIT and Published on GitHub  
699 <https://github.com/PatrickYLi/LAD-Regression/tree/multi-core> and Zenodo  
700 (doi/10.5281/zenodo.10836723)  
701

**702 References**

- 703 Anderson, R. J., and P. R. Griffiths (1975), Errors in absorbance measurements in infrared Fourier  
704 transform spectrometry because of limited instrument resolution, *Analytical Chemistry*, 47(14), 2339-  
705 2347, doi:10.1021/ac60364a030.
- 706 Baroni, M., J. Savarino, J. Cole-Dai, V. K. Rai, and M. H. Thiemens (2008), Anomalous sulfur  
707 isotope compositions of volcanic sulfate over the last millennium in Antarctic ice cores, *J. Geophys.*  
708 *Res. Atmos.*, 113(D20).
- 709 Baroni, M., M. H. Thiemens, R. J. Delmas, and J. Savarino (2007), Mass-independent sulfur isotopic  
710 compositions in stratospheric volcanic eruptions, *Science*, 315(5808), 84-87,  
711 doi:10.1126/science.1131754.
- 712 Barra, I., L. Khiari, S. M. Haefele, R. Sakrabani, and F. Kebede (2021), Optimizing setup of scan  
713 number in FTIR spectroscopy using the moment distance index and PLS regression: application to  
714 soil spectroscopy, *Scientific reports*, 11(1), 1-9, doi:10.1038/s41598-021-92858-w.
- 715 Blackie, D., R. Blackwell-Whitehead, G. Stark, J. C. Pickering, P. L. Smith, J. Rufus, and A. P.  
716 Thorne (2011), High-resolution photoabsorption cross-section measurements of SO<sub>2</sub> at 198 K from  
717 213 to 325 nm, *J. Geophys. Res.*, 116(E3), doi:10.1029/2010je003707.
- 718 Claire, M. W., J. F. Kasting, S. D. Domagal-Goldman, E. E. Stüeken, R. Buick, and V. S. Meadows  
719 (2014), Modeling the signature of sulfur mass-independent fractionation produced in the Archean  
720 atmosphere, *Geochimica et Cosmochimica Acta*, 141, 365-380, doi:10.1016/j.gca.2014.06.032.
- 721 Danielache, S. O., C. Eskebjerg, M. S. Johnson, Y. Ueno, and N. Yoshida (2008), High-precision  
722 spectroscopy of <sup>32</sup>S, <sup>33</sup>S, and <sup>34</sup>S sulfur dioxide: Ultraviolet absorption cross sections and isotope  
723 effects, *J. Geophys. Res. Atmos.*, 113(D17), doi:10.1029/2007JD009695.

- 724 Danielache, S. O., S. Hattori, M. S. Johnson, Y. Ueno, S. Nanbu, and N. Yoshida (2012),  
725 Photoabsorption cross-section measurements of  $^{32}\text{S}$ ,  $^{33}\text{S}$ ,  $^{34}\text{S}$ , and  $^{36}\text{S}$  sulfur dioxide for the  $B^1B_1-X^1A_1$   
726 absorption band, *J. Geophys. Res. Atmos.*, *117*(D24), doi:10.1029/2012jd017464.
- 727 Danielache, S. O., G. Iwama, M. Shinkai, M. Oinuma, E. Simoncini, and T. Grassi (2023),  
728 Introducing atmospheric photochemical isotopic processes to the PATMO atmospheric code,  
729 *Geochem. J.*, *57*(2), 42-58, doi:10.2343/geochemj.GJ23004.
- 730 Dreissig, I., S. Machill, R. Salzer, and C. Krafft (2009), Quantification of brain lipids by FTIR  
731 spectroscopy and partial least squares regression, *Spectrochimica Acta Part A: Molecular and*  
732 *Biomolecular Spectroscopy*, *71*(5), 2069-2075, doi:10.1016/j.saa.2008.08.008.
- 733 Eiler, J. M., B. Bergquist, I. Bourg, P. Cartigny, J. Farquhar, A. Gagnon, W. Guo, I. Halevy, A.  
734 Hofmann, and T. E. Larson (2014), Frontiers of stable isotope geoscience, *Chem. Geol.*, *372*, 119-  
735 143, doi:10.1016/j.chemgeo.2014.02.006.
- 736 Endo, Y., S. O. Danielache, and Y. Ueno (2019), Total pressure dependence of sulfur mass-  
737 independent fractionation by  $\text{SO}_2$  photolysis, *Geophys Res Lett*, *46*(1), 483-491,  
738 doi:10.1029/2018gl080730.
- 739 Endo, Y., S. O. Danielache, Y. Ueno, S. Hattori, M. S. Johnson, N. Yoshida, and H. G.  
740 Kjaergaard (2015), Photoabsorption cross-section measurements of  $^{32}\text{S}$ ,  $^{33}\text{S}$ ,  $^{34}\text{S}$ , and  $^{36}\text{S}$   
741 sulfur dioxide from 190 to 220 nm, *Journal of Geophysical Research: Atmospheres*, *120*(6),  
742 2546-2557, doi:10.1002/2014JD021671.
- 743 Endo, Y., S. O. Danielache, M. Ogawa, and Y. Ueno (2022a), Absorption spectra  
744 measurements at  $\sim 1 \text{ cm}^{-1}$  spectral resolution of  $^{32}\text{S}$ ,  $^{33}\text{S}$ ,  $^{34}\text{S}$ , and  $^{36}\text{S}$  sulfur dioxide for the  
745 206–220 nm region and applications to modeling of the isotopic self-shielding, *Geochemical*  
746 *Journal*, *56*(1), 40-56, doi:10.2343/geochemj.GJ22004.
- 747 Endo, Y., Sekine, Y., and Ueno, Y. (2022b). Sulfur mass-independent fractionation during  
748  $\text{SO}_2$  photolysis in low-temperature/pressure atmospheres. *Chemical Geology*, *609*, 121064.  
749 doi.org/10.1016/j.chemgeo.2022.121064
- 750 Endo, Y., Y. Ueno, S. Aoyama, and S. O. Danielache (2016), Sulfur isotope fractionation by  
751 broadband UV radiation to optically thin  $\text{SO}_2$  under reducing atmosphere, *Earth and*  
752 *Planetary Science Letters*, *453*, 9-22, doi:10.1016/j.epsl.2016.07.057.
- 753 Farquhar, J., H. Bao, and M. Thiemens (2000), Atmospheric influence of Earth's earliest sulfur cycle,  
754 *Science*, *289*(5480), 756-758, doi:science.289.5480.756.
- 755 Farquhar, J., J. Savarino, S. Airieau, and M. H. Thiemens (2001), Observation of wavelength-  
756 sensitive mass-independent sulfur isotope effects during  $\text{SO}_2$  photolysis: Implications for the early  
757 atmosphere, *Journal of Geophysical Research: Planets*, *106*(E12), 32829-32839,  
758 doi:10.1029/2000JE001437.
- 759 Gautier, E., J. Savarino, J. Erbland, and J. Farquhar (2018),  $\text{SO}_2$  oxidation kinetics leave a consistent  
760 isotopic imprint on volcanic ice core sulfate, *J. Geophys. Res. Atmos.*, *123*(17), 9801-9812.
- 761 Gueymard, C. A. (2004), The sun's total and spectral irradiance for solar energy applications and  
762 solar radiation models, *Solar energy*, *76*(4), 423-453, doi:10.1016/j.solener.2003.08.039.
- 763 Guo, S., Bluth, G. J. S., Rose, W. I., Watson, I. M., & Prata, A. J. (2004). Re-evaluation of  
764  $\text{SO}_2$  release of the 15 June 1991 Pinatubo eruption using ultraviolet and infrared satellite  
765 sensors. *Geochemistry, Geophysics, Geosystems*, *5*(4).  
766 <https://doi.org/10.1029/2003GC000654>

- 767 Hattori, S., J. A. Schmidt, M. S. Johnson, S. O. Danielache, A. Yamada, Y. Ueno, and N. Yoshida  
768 (2013), SO<sub>2</sub> photoexcitation mechanism links mass-independent sulfur isotopic fractionation in  
769 cryospheric sulfate to climate impacting volcanism, *Proceedings of the National Academy of*  
770 *Sciences*, 110(44), 17656-17661, doi:10.1073/pnas.1213153110.
- 771 Heicklen, J., N. Kelly, and K. Partymiller (1980), The photophysics and photochemistry of SO<sub>2</sub>,  
772 *Reviews of Chemical Intermediates*, 3(3-4), 315-404, doi:10.1007/bf03052425.
- 773 Herzberg, G. (1945), *Molecular spectra and molecular structure*, D. van Nostrand.
- 774 Hulston, J., and H. Thode (1965), Variations in the S<sup>33</sup>, S<sup>34</sup>, and S<sup>36</sup> contents of meteorites and their  
775 relation to chemical and nuclear effects, *J. Geophys. Res.*, 70(14), 3475-3484,  
776 doi:10.1029/JZ070i014p03475.
- 777 Koplow, J. P., D. A. Kliner, and L. Goldberg (1998), Development of a narrow-band, tunable,  
778 frequency-quadrupled diode laser for UV absorption spectroscopy, *Applied optics*, 37(18), 3954-3960,  
779 doi:10.1364/AO.37.003954.
- 780 Kostkowski, H. J., and A. M. Bass (1956), Slit function effects in the direct measurement of  
781 absorption line half-widths and intensities, *JOSA*, 46(12), 1060-1064, doi:10.1364/JOSA.46.001060.
- 782 Kroll, J. A., B. N. Frandsen, R. J. Rapf, H. G. Kjaergaard, and V. Vaida (2018), Reactivity of  
783 Electronically Excited SO<sub>2</sub> with Alkanes, *The Journal of Physical Chemistry A*, 122(39), 7782-7789,  
784 doi:10.1021/acs.jpca.8b04643.
- 785 Kumar, P., J. Ellis, and B. Poirier (2015), Rovibrational bound states of SO<sub>2</sub> isotopologues. I: Total  
786 angular momentum  $J=0-10$ , *Chem. Phys.*, 450, 59-73.
- 787 Leonard C. Entwicklung eines UV-laserspektroskopischen nachweisverfahrens für OH-  
788 Radikals und spektroskopische untersuchungen an spurengasen unter troposphärischen  
789 bedingungen, Germany: University of Hannover; 1989. Doctoral dissertation in physics.
- 790 Li, L., H. Zhao, N. Ni, Y. Wang, J. Gao, Q. Gao, Y. Zhang, and Y. Zhang (2022), Study on the origin  
791 of linear deviation with the Beer-Lambert law in absorption spectroscopy by measuring sulfur  
792 dioxide, *Spectrochimica Acta Part A: Molecular and Biomolecular Spectroscopy*, 275, 121192,  
793 doi:10.1016/j.saa.2022.121192.
- 794 Lyons, J., H. Herde, G. Stark, D. Blackie, J. Pickering, and N. de Oliveira (2018), VUV pressure-  
795 broadening in sulfur dioxide, *Journal of Quantitative Spectroscopy and Radiative Transfer*, 210, 156-  
796 164.
- 797 Masterson, A. L., J. Farquhar, and B. A. Wing (2011), Sulfur mass-independent fractionation patterns  
798 in the broadband UV photolysis of sulfur dioxide: Pressure and third body effects, *Earth and*  
799 *Planetary Science Letters*, 306(3), 253-260, doi:10.1016/j.epsl.2011.04.004.
- 800 Mellqvist, J., and A. Rosén (1996), DOAS for flue gas monitoring—II. Deviations from the Beer-  
801 Lambert law for the UV/visible absorption spectra of NO, NO<sub>2</sub>, SO<sub>2</sub> and NH<sub>3</sub>, *Journal of Quantitative*  
802 *Spectroscopy and Radiative Transfer*, 56(2), 209-224, doi:10.1016/0022-4073(96)00043-X.
- 803 Meyer-Jacob, C., H. Vogel, F. Boxberg, P. Rosén, M. E. Weber, and R. Bindler (2014), Independent  
804 measurement of biogenic silica in sediments by FTIR spectroscopy and PLS regression, *Journal of*  
805 *paleolimnology*, 52, 245-255, doi:10.1007/s10933-014-9791-5.
- 806 Ono, S. (2017), Photochemistry of sulfur dioxide and the origin of mass-independent isotope  
807 fractionation in Earth's atmosphere, *Annual Review of Earth and Planetary Sciences*, 45(1), 301-329,  
808 doi:10.1146/annurev-earth-060115-012324.
- 809 Origin, Version 2022. OriginLab Corporation, Northampton, MA, USA.

- 810 Pavlov, A., and J. Kasting (2002), Mass-independent fractionation of sulfur isotopes in Archean  
811 sediments: strong evidence for an anoxic Archean atmosphere, *Astrobiology*, 2(1), 27-41,  
812 doi:10.1089/153110702753621321.
- 813 Pedregosa, F., G. Varoquaux, A. Gramfort, V. Michel, B. Thirion, O. Grisel, M. Blondel, P.  
814 Prettenhofer, R. Weiss, and V. Dubourg (2011), Scikit-learn: Machine learning in Python, *The*  
815 *Journal of machine Learning research*, 12, 2825-2830.
- 816 Rufus, J., G. Stark, P. L. Smith, J. C. Pickering, and A. P. Thorne (2003), High-resolution  
817 photoabsorption cross section measurements of SO<sub>2</sub>, 2: 220 to 325 nm at 295 K, *Journal of*  
818 *Geophysical Research: Planets*, 108(E2), doi:10.1029/2002je001931.
- 819 Santos, V. H. J. M. D., D. Pontin, G. G. D. Ponzi, A. S. D. G. E. Stepanha, R. B. Martel, M. K.  
820 Schütz, S. M. O. Einloft, and F. Dalla Vecchia (2021), Application of Fourier Transform infrared  
821 spectroscopy (FTIR) coupled with multivariate regression for calcium carbonate (CaCO<sub>3</sub>)  
822 quantification in cement, *Construction and Building Materials*, 313, 125413,  
823 doi:10.1016/j.conbuildmat.2021.125413.
- 824 Savarino, J., A. Romero, J. Cole-Dai, S. Bekki, and M. Thiemens (2003), UV induced mass-  
825 independent sulfur isotope fractionation in stratospheric volcanic sulfate, *Geophys. Res. Lett.*, 30(21),  
826 doi:10.1029/2003GL018134.
- 827 Shaheen, R., M. Abauanza, T. L. Jackson, J. McCabe, J. Savarino, and M. H. Thiemens (2013), Tales  
828 of volcanoes and El-Niño southern oscillations with the oxygen isotope anomaly of sulfate aerosol,  
829 *Proceedings of the National Academy of Sciences*, 110(44), 17662-17667.
- 830 Skoog, D. A., F. J. Holler, and S. R. Crouch (2017), *Principles of instrumental analysis*, Cengage  
831 learning.
- 832 Stark, G., P. L. Smith, J. Rufus, A. Thorne, J. Pickering, and G. Cox (1999), High-resolution  
833 photoabsorption cross-section measurements of SO<sub>2</sub> at 295 K between 198 and 220 nm, *Journal of*  
834 *Geophysical Research: Planets*, 104(E7), 16585-16590, doi:10.1029/1999JE001022.
- 835 Tsai, S.-M., E. K. Lee, D. Powell, P. Gao, X. Zhang, J. Moses, E. Hébrard, O. Venot, V. Parmentier,  
836 and S. Jordan (2023), Photochemically produced SO<sub>2</sub> in the atmosphere of WASP-39b, *Nature*,  
837 617(7961), 483-487.
- 838 Ueno, Y., M. S. Johnson, S. O. Danielache, C. Eskebjerg, A. Pandey, and N. Yoshida (2009),  
839 Geological sulfur isotopes indicate elevated OCS in the Archean atmosphere, solving faint young sun  
840 paradox, *Proceedings of the National Academy of Sciences*, 106(35), 14784-14789,  
841 doi:10.1073/pnas.0903518106.
- 842 Vandaele, A. C., C. Hermans, and S. Fally (2009), Fourier transform measurements of SO<sub>2</sub> absorption  
843 cross sections: II.: Temperature dependence in the 29 000–44 000 cm<sup>-1</sup> (227–345 nm) region, *Journal*  
844 *of Quantitative Spectroscopy and Radiative Transfer*, 110(18), 2115-2126,  
845 doi:10.1016/j.jqsrt.2009.05.006.
- 846 Whitehill, A., and S. Ono (2012), Excitation band dependence of sulfur isotope mass-independent  
847 fractionation during photochemistry of sulfur dioxide using broadband light sources, *Geochimica et*  
848 *Cosmochimica Acta*, 94, 238-253, doi:10.1016/j.gca.2012.06.014.
- 849 Whitehill, A. R., C. Xie, X. Hu, D. Xie, H. Guo, and S. Ono (2013), Vibronic origin of sulfur mass-  
850 independent isotope effect in photoexcitation of SO<sub>2</sub> and the implications to the early earth's  
851 atmosphere, *Proceedings of the National Academy of Sciences*, 110(44), 17697-17702,  
852 doi:10.1073/pnas.1306979110.

853 Wu, C. R., B. Yang, F. Chen, D. Judge, J. Caldwell, and L. Trafton (2000), Measurements of high-,  
854 room-, and low-temperature photoabsorption cross sections of SO<sub>2</sub> in the 2080- to 2950-Å region,  
855 with application to Io, *Icarus*, *145*(1), 289-296, doi:10.1006/icar.1999.6322.  
856 Yung, Y. L., and W. B. DeMore (1999), *Photochemistry of planetary atmospheres*, Oxford University  
857 Press, USA, doi:10.1093/oso/9780195105018.001.0001.

858

859

860

861

862

863